Growth and global persistence of stratospheric sulfate aerosols from the 2022 Hunga Tonga-Hunga Ha'apai volcanic eruption

Marie Boichu[1], Raphael Grandin[2], Luc Blarel[1], Benjamin Torres[3], Yevgeny Derimian[4], Philippe Goloub[5], Colette Brogniez[6], Isabelle Chiapello[7], Oleg Dubovik[8], Théo Mathurin[9], Nicolas Pascal[9], Maximilien Patou[9], and Jérôme Riedi[10]

[1]CNRS/Université de Lille, Laboratoire d'Optique Atmosphérique, CNRS
[2]Université de Paris, Institut de physique du globe de Paris, CNRS
[3]Université de Lille, Laboratoire d'Optique Atmosphérique, CNRS
[4]University of Lille
[5]Lille University
[6]Univ. Lille, CNRS
[7]CNRS, Univ. Lille, Laboratoire d'Optique Atmosphérique
[8]CNRS, Universite Lille-1
[9]University of Lille, CNRS, CNES, UMS 2877 – ICARE Data and Services Center
[10]Laboratoire d'Optique Atmosphérique

February 22, 2024

Abstract

Stratospheric sulfate aerosols play a key role on atmospheric chemistry and Earth's radiation budget, but their size distribution, a critical parameter in climate models, is generally poorly-known. We address such gap for the 2022 Hunga Tonga-Hunga Ha'apai (HT-HH) volcanic eruption by exhaustively analyzing a set of satellite observations (TROPOMI, IASI, AHI, CALIOP) together with photometric ground observations from the worldwide open-access AERONET network. We document a rapid growth of HT-HH sulfate aerosols in the days following eruption, faster than observed for 1991 Pinatubo eruption, likely due to the exceptional hydration of the stratosphere by this phreatomagmatic eruption. An unusual aerosol fine mode (peak radius in 0.3-0.5 μm) is identified at 20 stations of the southern hemisphere until May 2023 (time of writing). Nevertheless, 1.4 years after eruption, HT-HH sulfate aerosols remain smaller than Pinatubo particles. Smaller aerosols backscatter more efficiently visible light and sediment more slowly than larger particles, implying stronger and longer-lasting negative radiative forcing.

Growth and global persistence of stratospheric sulfate aerosols from the 2022 Hunga Tonga-Hunga Haápai volcanic eruption

Marie Boichu[1,2], Raphaël Grandin[3], Luc Blarel[1,2], Benjamin Torres[2], Yevgeny Derimian[1,2], Philippe Goloub[2], Colette Brogniez[2], Isabelle Chiapello[1,2], Oleg Dubovik[1,2], Théo Mathurin[4], Nicolas Pascal[1,4], Maximilien Patou[4], Jérôme Riedi[2,4]

[1]CNRS, UMR 8518, F-59000 Lille, France
[2]University of Lille, UMR 8518 - LOA - Laboratoire d'Optique Atmosphérique, F-59000 Lille, France
[3]Université Paris Cité, Institut de Physique du Globe de Paris, CNRS, 75005 Paris, France
[4]University of Lille, CNRS, CNES, UMS 2877 – ICARE Data and Services Center, F-59000 Lille, France

Key Points:

- In the days following eruption, Hunga Tonga sulfate aerosols are observed to grow faster than Pinatubo particles.
- Hunga Tonga stratospheric aerosols persist for >14 months as identified at 20 AERONET stations of the southern hemisphere.
- One year after eruption, Hunga Tonga aerosols remain smaller than Pinatubo particles, potentially implying an enhanced climate impact.

Corresponding author: Marie Boichu, marie.boichu@univ-lille.fr

Abstract

Stratospheric sulfate aerosols play a key role on atmospheric chemistry and Earth's radiation budget, but their size distribution, a critical parameter in climate models, is generally poorly-known. We address such gap for the 2022 Hunga Tonga-Hunga Haápai (HT-HH) volcanic eruption by exhaustively analyzing a set of satellite observations (TROPOMI, IASI, AHI, CALIOP) together with photometric ground observations from the worldwide open-access AERONET network. We document a rapid growth of HT-HH sulfate aerosols in the days following eruption, faster than observed for 1991 Pinatubo eruption, likely due to the exceptional hydration of the stratosphere by this phreatomagmatic eruption. An unusual aerosol fine mode (peak radius in 0.3-0.5 μm) is identified at 20 stations of the southern hemisphere until May 2023 (time of writing). Nevertheless, 1.4 years after eruption, HT-HH sulfate aerosols remain smaller than Pinatubo particles. Smaller aerosols backscatter more efficiently visible light and sediment more slowly than larger particles, implying stronger and longer-lasting negative radiative forcing.

Plain Language Summary

Explosive eruptions can inject large amounts of sulfate aerosols in the stratosphere, that may perturb atmospheric chemistry and Earth's climate. However, crucial information regarding the size of aerosols, a critical parameter in climate models, is generally missing. We address this gap for the eruption of Hunga Tonga-Hunga Haápai (HT-HH) in 2022, a record-breaking eruption in the satellite era. Based on an exhaustive analysis of satellite observations together with photometric ground observations from the worldwide open-access AERONET network, we document a rapid growth of HT-HH aerosols in the days following eruption. This early aerosol growth rate is faster than observed for 1991 Pinatubo, likely due to the exceptional humidification of the stratosphere caused by the water-rich HT-HH eruption. Furthermore, the year-long persistence of an unusually fine type of aerosols (i.e. with radius $\sim$0.4 μm) is identified at 20 stations of the southern hemisphere and used as a volcanic marker of the HT-HH plume. One year after eruption, and in spite of an initially rapid growth, HT-HH sulfate aerosols remain smaller than Pinatubo particles. Smaller particles better reflect sunlight and remain in suspension in the stratosphere for a longer time, fostering surface cooling.

1 Introduction

Since the 1991 eruption of Pinatubo (Philippines, 15°N, 120°E), long-lived stratospheric sulfate aerosols produced by high-magnitude explosive eruptions are known to modify atmospheric chemistry, dynamics and Earth's radiation balance (McCormick et al., 1995; Robock, 2000; Kremser et al., 2016; Marshall et al., 2022).

The eruption of Hunga Tonga-Hunga Haápai (HT-HH, 20.5°S, 175.4°W, Fig. 1) in January 2022 represents a record-breaking eruption in the satellite era, whose impact on climate remains to be assessed. Its phreatomagmatic nature fueled an exceptional explosive activity, with plume parcels reaching up to 57 km of altitude (Carr et al., 2022; Taha et al., 2022; Proud et al., 2022), leading to the largest aerosol perturbation of the stratosphere since the Pinatubo eruption (Sellitto et al., 2022; Legras et al., 2022). Considerable amounts of water vapour injected high into the atmosphere induced exceptional hydration of the stratosphere (Millan et al., 2022; Schoeberl et al., 2022; Vömel et al., 2022) and modifications in atmospheric circulation (Coy et al., 2022). However, the modest mass budget of SO_2 emitted dur-

ing the paroxysmal phase of the eruption on 15 January 2022 (0.4-0.5 Tg, Carn et al. (2022), compared to ≈20 Tg during Pinatubo eruption, Bluth et al. (1992)), is in apparent contradiction with the strong explosivity of the eruption. Apart from potential bias in the satellite retrieval of SO_2 in presence of a large particle load in the plume, and acknowledging the probable amplification of explosivity due to magma-water interaction, this low SO_2 budget raises the possibility of a fast conversion of SO_2 into secondary sulfate aerosols.

The impact on climate of large eruptions can be evaluated with model simulations, but this approach is subject to uncertainty due to scarcity of direct observations of time-varying microphysical properties of stratospheric aerosols (Mann et al., 2015). Balloon-borne experiments are useful to provide direct constraints on the size distribution of stratospheric aerosols with altitude but, due to operational difficulty, cannot capture the detailed spatio-temporal evolution of aerosol microphysics (Deshler, 2008). Satellite occultation or limb-scattering measurements require prerequisite assumptions on particle size distribution or chemical composition (Wrana et al., 2021; Taha et al., 2021; Bourassa et al., 2023).

Here, we analyze open-access data from the AERONET ground network of photometers that provide, at >600 stations worldwide, information on the optical, microphysical and absorption properties of aerosols in the atmospheric column (B. Holben et al., 2001; Dubovik et al., 2002). Photometric observations have already provided information on the size distribution of volcanogenic stratospheric aerosols in the past decades. Originally, Asano et al. (1993) derived the radius of Pinatubo aerosols from spectral AOT measurements at one single station in Japan. Using volume size distributions retrieved at a few AERONET sites, B. Holben et al. (1996) and T. F. Eck et al. (2010) highlighted an unusual "middle mode" (between the usual fine and coarse modes) associated with Pinatubo aerosols. Stothers (2001) evaluated the post-eruption effective radius (r_{eff}) of fine aerosols from ground-based spectral extinction measurements for the seven largest aerosol-producing volcanic eruptions in the twentieth century. N. T. O'Neill et al. (2012) followed the properties of stratospheric sulfate aerosols from the 2009 Sarychev eruption using measurements from Eureka AERONET station and polar sites of Ny-Alesund and Opal. More recently, Ridley et al. (2014) highlighted the influence of moderate eruptions in the low stratosphere on the decadal trend in stratospheric aerosol optical depth (AOD).

Together with satellite observations (S5P/TROPOMI, MetOp-B and MetOp-C/IASI, HIMAWARI-8/AHI, CALIPSO/CALIOP), we analyse aerosol properties derived from photometric data collected at 20 stations of the southern hemisphere to characterize and track the persistence of volcanic aerosols associated with HT-HH eruption.

2 Observations and methodology

A set of observations of volcanic sulfur dioxide (SO_2) gas and particles, from passive sensors onboard low earth orbit and geostationary satellites as well as active spaceborne LIDAR, is analysed. It includes SO_2 vertical column amounts (15 km product) from high spectral and spatial resolution ultraviolet observations from Sentinel-5P/TROPOspheric Monitoring Instrument (TROPOMI) with a pixel size of 7 km x 3.5 km at nadir (Theys et al., 2017, 2019). SO_2 height products, derived from observations of the Infrared Atmospheric Sounding Interferometer (IASI) onboard MetOp-B and MetOp-C polar orbiting satellites (footprint of 12 km at nadir) (Clarisse et al., 2014), also allow us to track four times a day the HT-HH plume and over a longer period of time than using SO_2 column amounts. Near-source particle properties are explored using SEVIRI-like ash RGB compositions derived from geostationary L1B

brightness temperatures of HIMAWARI-8/AHI (Advanced Himawari Imager) at 8.6, 10.4 and 12.4 μm channels available every 20 minutes (EUMETSAT, 2023; Japan Meteorological Agency, 2023) as well as observations from the spaceborne CALIPSO/Cloud-Aerosol Lidar with Orthogonal Polarization (CALIOP) including total attenuated backscatter at 532 nm and depolarization ratio (Winker et al., 2009).

Regarding ground-based observations, we analyze cloud-screened Level 1.5 observations (version 3, Giles et al. (2019)) from the worldwide AERONET network of sun/sky radiometers (B. N. Holben et al., 1998; B. Holben et al., 2001), with a focus on a selected subset of 20 stations in the southern hemisphere. Quasi-continuous direct sun measurements, with a sampling interval of 5 to 15 minutes (under cloudless conditions), provide AOD and Angstrom exponent values (B. N. Holben et al., 1998; B. Holben et al., 2001) as well as the partition of AOD_{500nm} between fine and coarse mode particles using the SDA algorithm (N. O'Neill et al., 2003). Measurements are collected both in daylight and at night using lunar photometry (Barreto et al., 2016).

Using the same ground-based instruments, sky radiance measurements are also retrieved in the almucantar geometry (e.g. fixed elevation angle equal to solar elevation, and full 360° azimuthal sweep) at various wavelengths (440, 670, 870 and 1020 nm). These multi-angular and multi-spectral observations are modeled with a radiative transfer model combined with a microphysical description of light scattering by particles, and inverted using a procedure incorporating smoothness constraints on spectral and size distributions as well as a robust statistical noise model (Dubovik & King, 2000; Dubovik et al., 2002). The algorithm provides a detailed evaluation of the volume size distribution (VSD), absorption (single scattering albedo, SSA) and complex refractive index of aerosols (Dubovik & King, 2000; Dubovik et al., 2000, 2002, 2006; B. N. Holben et al., 2006; Torres et al., 2014). In Version 3 of the algorithm, aerosols are assumed to be partitioned into two classes including spherical and non-spherical components (Dubovik et al., 2006). The spherical component is modeled by polydispersed homogeneous spheres with the same complex refractive index. The non-spherical component is a mixture of polydisperse, randomly-oriented homogeneous spheroids. Importantly, accuracy of VSD retrieval is maintained for AOD_{440nm} down to 0.02, compared to AOD_{440nm}>0.4 for SSA (Sinyuk et al., 2020). Nevertheless, edges of the aerosol VSD (radius < 0.1 μm and $>$ 7 μm) are less constrained because of the low sensitivity of the aerosol scattering at the wavelengths that are measured for these sizes of aerosols. However, the size of HT-HH aerosols belongs to the range of aerosol size retrieved with the highest accuracy (retrieval error $< 10\%$ for maxima of the VSD, Dubovik et al. (2002)). In summary, even if less frequent than direct measurements due to restrictive quality criteria, almucantar measurements give access to the complete volume size distribution of aerosols with minimal constraints. Throughout the paper, selected data fulfill quality criteria (sky residual<10%, SZA<70°). A low sky residual ensures that aerosol properties are homogeneous at the scale of the Almucantar field of view.

In common atmospheric conditions, two local maxima of the VSD are found, classically referred to as the "fine mode" and the "coarse mode". The standard AERONET processing provides the effective radius for each mode, noted r_{eff}, which represents an integral quantity over each sub-distribution, eg. the ratio of the skewness to the variance of the particle number distribution (T. Eck et al., 1999). However, the effective radius brings a blurred vision in the case of overlapping size distributions within a specific mode (T. F. Eck et al., 2010), which may arise in the event of a volcanic eruption.

Alternatively, in order to identify the volcanic modes associated with HT-HH aerosols, we search for the local maxima of the aerosol VSDs after applying a spline interpolation. This

approach is intended to better achieve the detection and separation of sub-populations of aerosols that may coexist in the atmospheric column, regardless of the actual shape of the underlying size distribution. The method uses as input the almucantar-derived VSD provided by AERONET, noted v_j, sampled in 22 bins centered on radii r_j (where j is the index of the bin) with a regular logarithmic progression between 0.05 μm and 15.0 μm. A cubic-spline fitting of v_j is performed, yielding an interpolated spline object $\mathbf{f}$ (ie. a piecewice cubic polynomial function), such that $\mathbf{f}(r_j) = v_j, \forall j$. Note that $\mathbf{f}$ can be evaluated at any r in each $[r_j, r_{j+1}]$ interval, potentially overshooting slightly above v_j or v_{j+1}. Nevertheless, because the v_j are regularly spaced and already "smooth", the overshoot effect remains contained.

After interpolation, all local maxima of $\mathbf{f}$ on the $[0.05{-}15.0]\mu$m interval are calculated:

$$r_{peak} = \arg \underset{r \in S}{\text{localmax}}\, \mathbf{f}(r), \text{ with } S = [0.05, 15.0]\ \mu\text{m} \tag{1}$$

Local maxima occurring at interval endpoints (0.05 μm and 15.0 μm) are discarded a posteriori to avoid side effects. The number of remaining local maxima depends on the shape of v_j, and varies between one, when a single peak dominates the distribution, and, exceptionally, up to five. However, in most profiles, two local maxima are found, representing the fine mode and the coarse mode. After the HT-HH eruption, as discussed later, a third local maximum becomes visible on a number of stations.

When several peaks are found, they are sorted by decreasing order of their respective amplitude in the VSD. In other words, for each almucantar-derived VSD, the method extracts a list of local maxima of the interpolated VSD, indexed by integer i, each with a radius $r_{peak,i}$ and an amplitude $A_{peak,i}$. Hence, $r_{peak,1}$ is the radius of largest peak in the VSD with amplitude $A_{peak,1}$, then $r_{peak,2}$ is the second-largest peak with amplitude $A_{peak,2} < A_{peak,1}$, and so forth. The value of $A_{peak,i}$ is the "height" of the VSD for the mode corresponding to the peak with index i, and can be interpreted as a proxy of the particle abundance, for this particular peak, in the atmospheric column above the station. VSDs with more than three local maxima are found in situations with low particle abundance, close to the measurement noise, so that peaks with indexes $i \geq 4$ can be ignored. The width of the bins, which varies logarithmically with the radius, can be taken as a conservative estimate of the uncertainty of the retrieved r_{peak}. To give numerical values relevant to the HT-HH volcanic range, bin width increases from ~ 0.07 μm at $r_{peak} = 0.25\mu$m, to ~ 0.16 μm at $r_{peak} = 0.57\mu$m.

The joint interpretation of satellite and ground-based remote sensing observations of the HT-HH plume, as well as multi-station data analysis, are performed using the VOLCPLUME interactive web portal (Boichu & Mathurin, 2022), that was used in crisis time to deliver information on HT-HH aerosols (Vernier et al., 2022; Lac et al., 2022).

3 Results

3.1 Evolution of sulfate aerosols size during the first circumnavigation of the globe

3.1.1 Rapid growth (15–22 January 2022)

Near-source satellite and ground-based observations in Fig. 1 illustrate the spatio-temporal evolution of SO_2 and particles emitted by the explosive HT-HH eruption on 15 January 2022 until their overpass over Australian land surfaces that are instrumented with ground-based

sun/sky radiometers of the AERONET network. Joint comparison of satellite and ground-based data is essential to pinpoint the precise time of overpass by the plume, and associate unambiguously any anomaly in ground measurements to a volcanic origin.

The explosive eruption of HT-HH starts on 15 January 2022 around 04:00 UTC (Fig. 1a1), according to the first plume detection illustrated by Himawari-8/AHI observations at 04:20 UTC (Fig. S1 and Movie S1). Coarse particles near the volcanic source are highlighted by dark colors (brownish/blue/black) in ash RGB compositions (Fig. 1a1 and a2) indicating presence of ice crystals, sea salts or coarse ash particles (EUMETRAIN, 2023). A rapid change in plume characteristics, shifting from dark (Fig. 1a1 and 1a2) to light green (Fig. 1a3 and 1a4) colors, indicates a predominant abundance of SO_2 and sulfate aerosols in the HT-HH plume (e.g. from 16 Jan 2022 00:00 UTC, Fig. 1a3), supporting near-source modification of the physico-chemical properties of the HT-HH plume. This change may explain the disappearance of coarse particles, possibly resulting from sedimentation/wet aggregation processes (Textor et al., 2006; Folch et al., 2010) and/or dilution of the dispersed plume inducing a decaying signal from small ash particles (<few microns) below the detection threshold of geostationary infrared observations (Prata, 1989), as also discussed by Legras et al. (2022).

TROPOMI observations on 17 January (from 00:00 to 05:00 UTC) confirm quantitatively the detection of the SO_2-rich HT-HH plume reaching Australia (Fig. 1b), so far qualitatively imaged with Himawari-8/AHI (Fig. 1a4). Approximately ten hours before this TROPOMI acquisition (16 January 15:41 UTC), CALIPSO/CALIOP observations detect aerosols in the HT-HH plume passing over the Coral Sea (Fig. 1d). CALIOP observations indicate that the plume is mainly composed of poorly-depolarizing (e.g. almost spherical, depolarization ratio <3%, Fig. S2) aerosols in the stratosphere, hence suggesting a young plume already rich in sulfate aerosols. The vertical distribution of HT-HH aerosols is complex with distinct parcels at, at least, two distinct altitudes (Fig. 1d): one parcel at 26-29 km asl (with a weaker signal indicating presence of aerosols around 23-24 km), another parcel, further south, at 30-32 km asl. Nevertheless, we cannot exclude the presence of aerosols at a higher altitude at that time, with potentially different properties. Indeed, CALIOP detected higher altitude aerosols (between 35-40 km) earlier on 15 January with strongly depolarizing properties supporting the presence of ash and/or ice (Khaykin et al., 2022). Taha et al. (2022) also report the presence of such high altitude aerosols (>36.5 km) over Australia on 17 January from OMPS-LP observations. The persistence of volcanic aerosols at altitudes >36 km is observed with OMPS-LP up to 27 January 2022 with a decaying aerosol extinction ratio anomaly (Taha et al., 2022). However, OMPS-LP data do not provide information on the depolarizing properties of these transient high-altitude particles.

Eastern Australia hosts the first AERONET photometric station (Lucinda) flown over by the plume (Fig. 1c). By analysing the aerosol volume size distributions coinciding with the SO_2 plume overpass, along with the AOD partitioning between fine and coarse mode, detailed information on the microphysical and radiative properties of HT-HH aerosols can be deduced (Fig. 2). An excess AOD anomaly peaking at about 2 (at 440 nm) is recorded on late 16 January 2022 at 21:36 UTC, largely above background values (Fig. 1c). These high AOD values are mainly caused by fine particles (radius <0.5 μm) (Fig. 2b2), while the coarse AOD only slightly departs from background (Fig. 2b3, see also Section 4.2). Inversions of almucantar observations, collected on 16 January 2022 at 22:10 and 22:36 UTC, confirm the abundance of fine particles, with volume concentrations greater by a factor of ≈ 30 relatively to background conditions (Fig. 2c). However, their size (r_{eff} ranging in 0.22-0.23 μm, Fig. 2c) is significantly larger than background aerosols observed before the plume overpass (0.12 μm), exceeding the historical monthly-mean ($\pm 1\sigma$) range (0.11–0.17 μm, blue shaded area

in Fig. S3.1). Furthermore, these fine aerosols are poorly-absorbing, with a SSA_{440nm} ranging in 0.97-0.98, much higher than recorded early morning 12 hours before the HT-HH plume overpass (SSA_{440nm} of 0.85), and in the upper bound of historical monthly-mean SSA values (0.78–0.98, red shaded area in Fig. S3.1). Given $AOD_{440nm} >> 0.5$, the complex refractive index of these aerosols can be retrieved, with a real part shown to vary between 1.33 at 440 nm and 1.35 at 1020 nm and a constant imaginary part ranging in 0.003–0.004. Therefore, the abundant presence of poorly-absorbing fine aerosols indicates high concentrations of sulfate aerosols within the HT-HH young plume (about 42 hour-old plume).

On 19 January, a broader peak in AOD_{500nm}, reaching ≈ 1, lasting about 12 hours, is recorded in western Australia (Learmonth), 7000 km from source (Fig. 2b). The plume then reaches the stations of Maido OPAR and Saint-Denis on La Réunion island on 21 January (Fig. 2a2), 13000 km from source, with an AOD_{500nm} up to 0.6 for two days (Fig. 2b). The timing of the AOD peak detection at stations Lucinda, Learmonth and Maido is consistent with the translation of the volcanic plume visible in SO_2 satellite imagery (Fig. S4). Furthermore, the broadening of the AOD peak toward the west, as well as the decrease of the peak amplitude toward the west, are consistent with a progressive elongation and dispersion of the plume during transport over the Indian Ocean.

Whichever the station, these high total AOD values are mainly caused by fine particles (Fig. 2b). Again, a few almucantar observations provide detailed volume size distribution and absorption properties of aerosols measured over each station (Fig. 2c). In western Australia (Learmonth), fine mode r_{eff} of 0.33 μm is recorded on 19 January 2022, much larger than monthly-mean background values (0.14–0.20 μm, Fig. S3.2), with SSA_{440nm} of 0.98 far exceeding the monthly background (0.82–0.93, Fig. S3.2). A few days later on 22 January 2022, fine mode aerosols with r_{eff} of 0.39 μm are observed in La Réunion (Maido OPAR), much larger than monthly background values (0.12–0.23 μm), with SSA_{440nm} of 0.98 (Fig. S3.3). These observations indicate the growth of an unusual fine mode of poorly-absorbing particles, likely sulfates, almost doubling in size over their 7-days transport from eastern Australia (Lucinda) to La Réunion.

3.1.2 Stabilization of particle size (22–31 January 2022)

One week following the eruption, zonal progression of the HT-HH plume can be tracked by the successive occurrence of excess AOD anomalies, sweeping across the global ground-based AERONET network from east to west. Fig. 3 shows the spatio-temporal evolution of detections of excess fine AOD anomalies for a subset of nine AERONET stations situated within a latitudinal belt roughly centered on 20°S, which are all overpassed during the first circumnavigation of the globe by the SO_2-rich plume. To select these stations, we first systematically examined the pre- and post-overpass records at all stations in the 10°–30°S latitudinal band, and searched for an anomaly in properties of the fine mode, ie. affecting simultaneously both the AOD and the effective radius. Successive SO_2 maps produced by satellite imagery allowed us to correlate these anomalies with the presence of the volcanic plume. However, SO_2 conversion, in addition to dispersion and to dry/wet deposition, leads to decaying SO_2 concentrations in satellite products (Fig. S4). Hence, in order to facilitate the ground-to-satellite comparison, instead of TROPOMI SO_2, we used SO_2 detections derived from bi-daily IASI SO_2 height products (Clarisse et al., 2014). For the aged plume (ie. 1 week – 2 weeks after eruption), we found that IASI SO_2 height products achieve a lower detection threshold than TROPOMI SO_2 column amounts, and therefore bring a greater confidence for tracking the time of overpass of the dispersed HT-HH plume above ground stations (Fig. 3a).

In Africa, the first excess fine AOD anomalies are detected by AERONET stations in Mozambique (Niassa) on 21 January, then in Namibia and South Africa on 24–25 January (Windpoort, Metsi, Gobabeb) (Fig. 3b). Anomalies are then detected first on 26 January along the Atlantic coast of Brazil (SP-EACH), and finally on the Pacific side of the South American continent (PSDA-Chile) (Fig. 3b). To the extent made possible by the uneven temporal resolution involved in the correlation between SO_2 satellite images (revisit time of 12 hours for IASI) and direct sun measurements by ground stations, we find that the timing of detection of fine AOD anomalies from the ground coincides precisely with the overpass by the stratospheric HT-HH plume (Fig. 3). For a given longitude, the lag between stations located at different latitudes is well explained by the complex shape of the plume, as illustrated in Fig. 3a and Fig. 4 for Metsi station (South Africa).

The temporal coincidence between (a) detection of an anomaly in fine AOD from ground-based AERONET measurements, and (b) overpass by the SO_2 plume (as deduced from satellite imagery) indicates that ground-based AERONET measurements can be exploited to provide quantitative information about the characteristics of volcanic aerosols in the stratosphere, in particular their size thanks to almucantar inversions. For a number of stations in Africa and South America, a jump in the fine mode effective radius r_{eff} is distinctly visible in the time-series (Fig. 3c), coinciding with a notable excess in fine mode AOD (Fig. 3b). The anomaly is not visible at all stations, due to variability in the background records (pre-overpass) and/or gaps in the records (lack of almucantar observations at the time of overpass by the plume). At stations in Africa (Niassa, Metsi, Windpoort and Gobabeb) and in South America (SP-Each, PSDA Chile), we observe fine mode r_{eff} ranging in 0.24-0.4 μm during the plume overpass (Fig. 3c). We found that a threshold of r_{eff} >0.22 μm was sufficient to detect the time of appearance of the HT-HH overpass on the subset of nine stations (Fig. 3c). However, the fine mode effective radius cannot be considered as a reliable indicator of the size of volcanic particles when different populations of fine particles coexist within the atmospheric column.

In Fig. 4, we illustrate such a case with the African station of Metsi. Before the overpass of the station by the HT-HH plume (illustrated by IASI SO_2 detections in Fig. 4b), aerosol VSDs on 24 January (green-blue lines in Fig. 4a) indicate the presence of very fine aerosols with r_{eff} = 0.15–0.16 μm (Fig. 4c). One day later (25 January), as the HT-HH plume flies over the station (Fig. 4b), the particle size distribution shows the presence of a new aerosol mode of volcanic origin in the fine range, in addition to the very fine mode characteristic of "background" aerosols (orange line in Fig. 4a). This volcanic mode is, at this time, more abundant than the background mode. However, only a slight increase of the fine mode effective radius is observed, reaching only 0.24 μm (Fig. 4c).

Therefore, instead of relying on r_{eff}, we seek for anomalies in the location of the peaks in the VSD, which is a more reliable indicator in the presence of two (or more) sub-populations with overlapping distributions. In such a situation, contrary to the fine mode r_{eff}, the aerosol parameter r_{peak} (defined in Section 2) allows for separating the two populations, by providing a more accurate estimate of the volcanic aerosol radius $r_{peak-volc}$ and possibly also the background aerosol size $r_{peak-background}$. The $r_{peak-volc}$ parameter is expected to be very similar to the effective radius $r_{eff-volc}$ associated purely with the population of volcanic aerosols that can directly be measured with other methods such as in situ measurements. This approach is applied systematically for the identification of HT-HH sulfate aerosols over Africa and South America. The strategy involves finding the radius r_{peak} of the aerosols giving the largest contribution to the VSD fulfilling quality criteria (AOD>0.1, sky residual<10%).

At Metsi, this method highlights the coexistence of two distinct classes of fine aerosols on 25 January: (1) a very fine mode with $r_{peak-background} = 0.12$ μm, a value similar to the effective radius measured in background conditions, and (2) a larger fine mode of volcanic origin with $r_{peak-volc} = 0.45$ μm (Fig. 4c). The next day (26 January), the radius of the volcanic particles remains similar, with $r_{peak-volc}$ ranging in 0.39-0.42 μm (Fig. 4c).

Globally, after a rapid growth of sulfate aerosols almost doubling in size from eastern Australia to La Réunion, no further growth of HT-HH aerosols is observed over Africa or South America (Fig. 5). From 24 to late January 2022, stations in Africa, and then in South America, indicate aerosol $r_{peak-volc}$ slightly smaller (ranging in [0.36–0.47] μm) than at La Réunion (0.46 μm). Hence, although HT-HH plume gets more dispersed and diluted with time, in coherence with broadly decaying SO_2 concentrations and decreasing fine AOD (Fig. 3b), the size of the volcanic fine aerosols remains relatively stable (Fig. 5). Slight differences in aerosol size among different stations probably results from complexity in plume spatial distribution, in terms of SO_2/aerosol/water concentration and altitude, possibly reflecting some second-order heterogeneity in growth rate and composition.

3.2 Year-long persistence of HT-HH sulfate aerosols in southern hemisphere

From February 2022 to May 2023 (time of writing), we seek for the presence of an anomaly, presumably of volcanic origin, by analyzing the aerosol VSD derived from AERONET almucantar measurements. Fig. 6 displays the temporal evolution of aerosol VSD at La Réunion/Maido OPAR station, a high-altitude station (2160 m a.s.l.) in the Indian Ocean with a relatively pristine atmosphere (Koren et al., 2014). The volcanic signature is manifested by a change in the shape of the VSDs at the time of the eruption, with the emergence of a new mode, hereafter called "volcanic fine mode" or "volcanic mode", situated in the interval between the traditionally observed "fine" and "coarse" modes (Fig. 6a). This rare feature in the AERONET database is reminiscent of the "middle mode" previously documented for Pinatubo aerosols (B. Holben et al., 1996; T. F. Eck et al., 2010) and for desert dusts in Niger and Bodele Depression of central Chad (Tanré et al., 2001; T. F. Eck et al., 2010).

The volcanic mode produces an additional local maximum r_{peak} in the VSD around 0.4 μm, which can be tracked with time, as shown in Fig. 6b for station La Réunion/Maido OPAR. There, the r_{peak} anomaly is first visible on 22 January during the first HT-HH plume overpass (★ in Fig. 6, as discussed in Section 3.1.1). Then, after a temporary lull as the plume makes its first circumnavigation around the globe (♦ in Fig. 6), the volcanic anomaly becomes visible again from 9 February 2022 (♣ in Fig. 6). After February 2022, the volcanic aerosol fine mode anomaly remains continuously visible in the VSDs of La Réunion/Maido OPAR up to May 2023 (time of writing). The anomaly is also identified by comparing the density frequency histograms of aerosol radius in the fine range before and after the eruption (right hand side of Fig. 6b). The year-long persistence of this volcanic mode, here documented at the AERONET station of La Réunion/Maido OPAR, is consistent with LIDAR ground-based observations performed at the same observatory, which detect HT-HH aerosols in November 2022 (Baron et al. (2023) and pers. comm. from V. Duflot).

More broadly, manual search in the AERONET dataset reveals that the volcanic mode is detected at a total of (at least) 20 stations (including Maido OPAR) of the southern hemisphere (Fig. 7). These stations are located at latitudes ranging from 12°S (Mozambique/Niassa) to 46°S (Argentina/CEILAP Comodoro), in different continents and regions (Africa, South America, Australia, western Pacific region), and contrasted atmospheric environments. Us-

ing the same representations as in Fig. 6, VSDs (covering both fine and coarse modes) are shown at all 20 stations in Fig. S6 and the time-series of r_{peak} in Fig. S7 to S9.

This volcanic mode, with r_{peak} ranging in [0.28–0.50] μm, persists after eruption for a minimum of 16 months (at the time of writing). It is distinct from background fine mode aerosols visible in the months prior to eruption, which have generally a smaller size (<0.30 μm). However, in periods of enhanced background aerosol load, the volcanic signal may be temporarily lost. For instance, at Maido OPAR, as well as other stations in the Southern part of Africa (Fig. S8), the background aerosol load increases every year from September to November, temporarily obscuring the volcanic mode (♠ in Fig. 6). This period of enhanced AOD likely results from long-range transport of aerosols from biomass burning fires in southern Africa (and possibly Madagascar), which have been shown to impact ozone and carbon monoxide concentrations at La Réunion at that time of the year (Randriambelo et al., 2000; Clain et al., 2009; Foucart et al., 2018). On the other hand, detection is achieved even at stations affected by high levels of desert dust and/or sea salt (eg., Australia/Learmonth, Namibia/Gobabeb, Fig. 7 and S6), suggesting that the HT-HH volcanic signal is less perturbed by the presence of coarser particles.

For all four stations with enough data situated to the south of ∼33°S (AU NSW Lidcombe, Univ of Auckland, Trelew, CEILAP-Comodoro), the volcanic mode becomes visible in the time series of r_{peak} only after a time lag of several months, e.g. 3 months after eruption over Australia/AU NSW Lidcombe station (34°S) and 4 months over Argentina/Trelew station (43°S) (Fig. 7). At these stations, the time lag is also visible in the amplitude of the maximum of the VSD in the volcanic fine range (0.22–0.90 μm), which also increases from April–June 2022 at these southerly stations. This coincidence indicates an increase of the aerosol load in the atmospheric column prompted by the progressive influence of the HT-HH aerosols (Fig. S10). This latency for high-latitude stations suggests that it takes several months for the plume to reach high (southern) latitudes.

In order to assess the temporal variations of the HT-HH aerosol properties at the scale of the southern hemisphere, we stack observations from all 20 stations of Fig. 7. We first stack the amplitudes A_{peak} of the peaks falling within the volcanic mode size range, ie. [0.22–0.90 μm] (Fig. 8a). This "amplitude stack" can be interpreted as a proxy of the evolution of the column-integrated abundance of volcanic particles across the southern hemisphere. Only the radii falling with the interval [0.22–0.90 μm] are considered in the stack, in order to avoid interference with the non-volcanic fine or coarse background aerosols. We also stack the aerosol radii $r_{peak,i}$ at these 20 stations (Fig. 8b). These stacks show that, from the eruption until May 2023 (time of writing), HT-HH aerosol r_{peak} values range in 0.35-0.5 μm (Fig. 8b). Until June 2022, an overall decrease in particle size is observed (Fig. 8b), coinciding with an order of magnitude decrease in A_{peak} (Fig. 8a). During the same period of time, the scatter between values of r_{peak} at different stations tends to decrease, giving way to a narrow band in the stack of r_{peak} (dashed lines in Fig. 8b). Concomitantly, after June 2022, the amplitude A_{peak} in the volcanic range stabilizes to a nearly constant value of 0.005 $\mu m^3.\mu m^{-2}$ for all stations (Fig. 8a). This behavior likely reflects the progressive homogeneization of the HT-HH aerosol layer from January to June 2022, as VSDs at stations affected by the volcanic fingerprint tend to converge to a common shape and amplitude, hence yielding a geographically-uniform peak radius and peak amplitude. Given the spatial distribution of the stations, this hypothesis of an homogeneization of the HT-HH aerosol layer most likely extends to the scale of the southern hemisphere, at least down to 45°S. Accordingly, this strategy is warranted by the consistency of anomalies among selected stations, which allows for overcoming the existence of data gaps in individual time-series.

After June 2022, slow temporal variations of the HT-HH aerosol size are observed (Fig. 8b), with a minimum radius of 0.35 μm reached in July 2022, followed by a progressive increase up to 0.50 μm in late January 2023, and finally a slight decrease up to May 2023 (time of writing). The change of r_{peak} in late January 2023 appears to coincide with a drop of the amplitude A_{peak}, whose origin is uncertain due to lack of hindsight. Understanding the origin of these second order fluctuations would require further investigation.

4 Discussion

4.1 Estimated ranges of HT-HH aerosol size

In the 1 year-long timeseries of HT-HH sulfate aerosol size derived from AERONET photometric observations at 20 stations in the southern hemisphere, we report the detection of a volcanic fine mode with sub-micronic size (Fig. 8). The smallest particles, with a peak radius in 0.22-0.26 μm, are observed in Eastern Australia, $\sim$ 1 day after eruption (Fig. 2, 3 and 5), whereas particle size in subsequent measurements stabilizes to $\sim$ 0.4–0.5 μm within $\sim$ 1 week after the eruption (Fig. 5).

Comparison with other studies can be attempted on the basis of these size estimations, but requires careful consideration of the time and space frame of the comparison, as well as an understanding of uncertainties underlying each analysis. AERONET measurements provide estimates of size distribution integrated over the vertical column, hence do not allow for constraining the vertical distribution of aerosol properties. Furthermore, AERONET measurements are, by nature, punctual in space and intermittent in time. Hence, spatial heterogeneity of the HT-HH plume in the first weeks following the eruption precludes a direct translation of ground-based observations into averaged properties of the plume, which can only be achieved once the plume has homogenized. Based on the temporal evolution of HT-HH aerosol radius (estimated from r_{peak}), we estimate that this transient phase lasted for $\sim$ 4 months after the eruption (Section 3.2). Hence, until June 2022, heterogeneity of the aerosol layer may be easily invoked to explain, at least partly, any discrepancy between independent estimations of HT-HH aerosol properties. Nevertheless, the early stability of the aerosol radius, visible as early as $\sim$ 1 week after the eruption, elicits the comparison with previous studies that focused specifically on HT-HH aerosol size.

Based on AERONET observations, we measure an aerosol peak radius of 0.46 μm (r_{eff} of 0.39 μm) at La Réunion/Maido OPAR station on 22 January 2022 (Fig. 2c). This result is in broad agreement with the sub-micronic size of HT-HH aerosols derived from balloon-borne LOAC in situ measurements, collected a few days later on 23 and 26 January 2022 at La Réunion (Kloss et al., 2022). Nevertheless, we also find at La Réunion/Maido OPAR an unusual aerosol coarse mode that is characterized by r_{eff} of 4.6 μm on 22 January (Fig. S3.3). This is in line with a conspicuous spike in the coarse AOD at the neighboring AERONET station of Réunion St-Denis on 22 January 2022, around 02:00 UTC (Fig. 2b3). The absence of supra-micronic particles in Kloss et al. (2022) is only representative of measurements at their altitude of sampling (19–22 km altitude) and does not preclude the simultaneous presence of possibly larger particles traveling at higher or lower altitude. The coarse particles, with r_{eff} of 4.6 μm at La Réunion, are not found in later measurements, possibly indicating the presence of a transient parcel, consistent with the relatively heterogeneous plume observed in the first days following the eruption. A more in-depth discussion of this scenario is provided in Section 4.2.

Another approach for estimating HT-HH aerosol size consists in attributing the decrease of aerosol height with time to gravitational settling. Time-series of aerosol height are derived from satellite measurements, such as CALIOP (Legras et al., 2022) and OMPS-LP (Schoeberl et al., 2022; Khaykin et al., 2022). The height of the HT-HH stratospheric aerosol layer is shown to slowly descend from $\sim$ 24–26 km in February 2022 to $\sim$ 21–24 km in July 2022. This descent rate is then used to derive aerosol size estimations integrated over several months, based on a number of assumptions. First, when aerosol and water plumes overlap, the air vertical motion is determined by evaluating the ascent rate of the water plume, usually from MLS observations. When aerosol and water plumes do not overlap, Legras et al. (2022) use diabatic and adiabatic ERA5 vertical velocities instead. Secondly, they subtract the air motion to the aerosol descent rate so as to estimate the net aerosol sedimentation velocity. Thirdly, a simplified model for particle fall speed is used to evaluate aerosol size from settling rate using Stokes formula. Using this approach, preliminary analyses have estimated aerosol radii greater than 1 μm, which are hard to reconcile with our results: Schoeberl et al. (2022) report a radius of 1.2 μm in March–June 2022, whereas Legras et al. (2022) estimate a decrease from 2 μm in February 2022 to 0.5 μm in late July 2022. In contrast, a more recent study by Khaykin et al. (2022) yields a smaller aerosol radius of 0.35–0.54 μm in April-May 2022, which is fully consistent with our findings.

Lastly, evaluation of monthly-mean aerosol size is provided by fitting a lognormal size distribution to SAGE-III/ISS satellite extinction spectra (Khaykin et al., 2022). The information content of such spaceborne observations is insufficient to retrieve simultaneously aerosol size and composition as they both affect spectra inversion. For this reason, the distribution with altitude of the monthly-mean aerosol effective radius, averaged for a range of latitude in 10-30°S, is provided assuming different aerosol compositions with varying content of water and sulfuric acid (H_2SO_4). This results in an uncertainty of 0.1 μm, with HT-HH particle effective radius ranging within 0.4–0.5 μm from March to July 2022, as also reported by Duchamp et al. (2023), and hence in agreement with the aerosol size obtained from our analysis of AERONET data.

4.2 A potential signature of volcanic ash in the coarse mode

Following the discussion on the size of the fine mode particles (Section 4.1), we discuss further the coarse mode properties of the HT-HH plume during its first circumnavigation of the globe. Indeed, based on size distributions, a secondary peak in the coarse mode is detected by photometric data, possibly indicating the presence of coarse ash particles, albeit at an unknown altitude.

Concurrently with the fine mode fingerprint of volcanic aerosols associated with the HT-HH plume, a small excess in the coarse contribution to AOD, compared to background values, is observed at Lucinda (eastern Autralia) in the days following the peak in AOD, from 17 to 23 January 2022 (Fig. 2b3 and S11b). Unfortunately, only 4 almucantar-derived aerosol VSDs are available for that station at that time (Fig. S11c). These few VSDs nevertheless indicate a slightly larger coarse mode, with an effective radius r_{eff} ranging in 3.2–3.3 μm on late 16 January 2022, compared to measurements collected in the early morning of 16 January (before the HT-HH plume overpass) indicating a coarse mode r_{eff} of 1.9 μm (Fig. S3.1). Coarse particles on 16 January present a significantly larger size than coarse aerosols usually observed at Lucinda, as shown by historical monthly-mean values ($\pm 1\sigma$) at Lucinda which range in 1.6–2.3 μm (blue shaded area in Fig. S3.1). When the tail of the HT-HH plume passes over Lucinda four days later, on 20 January 2022, r_{eff} comes back down to 2.0–2.1 μm, hence

still remaining in the upper bound of commonly measured values for coarse aerosols at the station. Nevertheless, the coarse mode shape measured during HT-HH plume overpass is not statistically different from the coarse mode commonly measured at Lucinda, as shown by the climatological analysis of VSDs collected from 2009 to 2021 (selected with an Angstrom exponent < 0.5 to retain only abundant coarse particles, see dashed black line in Fig. S11c). We also note the absence of an unusual coarse mode (within the monthly-mean range) when the HT-HH plume passes a few days later over the station of Learmonth in western Australia (Fig. S3.2). Therefore, the volcanic origin of the coarse mode measured in Australia during HT-HH plume overpass remains inconclusive, as we cannot exclude that it originates from confounding non-volcanic sources, such as sea salts or desert dusts.

In contrast, at La Réunion, poorly-absorbing coarse particles with an unusually large size are recorded when the HT-HH plume passes over Maido OPAR, associated with r_{eff} of 4.6 μm on 22 January 2022 exceeding monthly values ranging in 1.6–3.8 μm in January (Fig. S3.3). An enhanced coarse mode AOD is also detected at St-Denis Réunion station the same day (Fig. 2b3). Concurrently, ground-based LIDAR observations performed at Maido OPAR during the previous and following nights (respectively, 21-22 January and 22-23 January) detect thick and dense volcanic layers from HT-HH at an altitude between 27-30 km (21-22 January) and 24-28 km (22-23 January), respectively (Baron et al., 2023; Khaykin et al., 2022). These layers present unusually large negative Angstrom exponents (of ≈ -0.8), indicating the significant presence of coarse particles (Baron et al., 2023). Therefore, both AERONET and LIDAR observations suggest the presence of coarse particles of volcanic origin over La Réunion on 22 January 2022.

Taken together, these observations are best explained by the presence of coarse ash particles affected by sulfate coating, producing particles with sulfate-like absorbing properties, and traveling coevally with smaller sulfate aerosols. This volcanic signature in the coarse mode is observed only during the first HT-HH plume overpass at La Réunion (Maido OPAR) on 22 January, and to a lesser extent in the younger plume at the Australian stations of Lucinda and Learmonth from 16 and 20 January.

The predominance of aerosols with low-depolarization properties measured with CALIOP after 15 January 2022 would be in agreement with this interpretation, as the coating of ash particles by sulfate likely leads to a spherical shape, especially for 7-day old particles at La Réunion. However, according to Legras et al. (2022) and Khaykin et al. (2022), these depolarizing properties are carried by small particles, and ash is believed to have been "washed out within the first day following the eruption" (Legras et al., 2022). In reality, when traveling in a dense SO_2- and sulfate-rich environment, finer ash particles are likely to stealthily remain in suspension as sulfate-coated ash particles, making them hard to distinguish from more chemically-pristine sulfate droplets. Furthermore, spatial heterogeneity within the plume in the first days post-eruption may not be fully sampled by lidar transects. This is in keeping with the presence of two isolated plume parcels with depolarizing properties (>50%) in the 16 January 2023 CALIOP transect at an altitude in 26-28 km (Fig. S2). Determining with confidence the actual fate of sulfate-coated ash particles over a time-scale of the order of a week would require more observations, which are unfortunately lacking.

4.3 Comparison with Pinatubo eruption: contrasting aerosol growth rates

We document in our study the gas to particle conversion of sulfuric species in the HT-HH plume, with SO_2 being oxidized to form stratospheric sulfuric acid aerosols. Their peak radius, quantified by analysis of photometric data, almost doubles from 0.24 μm (eastern Aus-

tralia, Lucinda) to 0.46 μm (La Réunion) in six days (Figures 2 and 5). An initial increase of the aerosol size was already reported by Khaykin et al. (2022), albeit over a longer time scale ($\sim$ 1 month), likely due to different spatio-temporal sampling and sensitivity. We also show that HT-HH aerosols reach a relatively stable size with r_{peak} of 0.35-0.45 μm less than two weeks after eruption (Fig. 5). Aerosol size then remains stable at 0.3-0.5 μm, with a mean value around 0.4 μm over the 1.3 years after eruption (Fig. 8b).

Given the importance of aerosol size in the climate impact of large volcanic eruptions, we aim at comparing the evolution in time of HT-HH aerosol size with the 1991 Pinatubo eruption (VEI 6). Unfortunately, lack of AERONET data prior to mid-1993 (birth of the network) prevents the application of the same methodology to retrieve Pinatubo aerosol (peak) radii in the two years after eruption. For this period of time, Russell et al. (1996) compiled a large variety of in situ and remote measurements allowing for describing the evolution of Pinatubo aerosol effective radius until August 1993 (Fig. 8c), in agreement with other ground-based spectral extinction observations later gathered by (Stothers, 2001). Two years after eruption, a middle mode peak associated with r_{eff} of 0.56 μm was highlighted from observations at two AERONET stations in the USA and Brazil in June 1993 (B. Holben et al., 1996; T. F. Eck et al., 2010), in agreement with retrievals from spectral AOD at a single Japanese station from January to April 1992 (Asano et al., 1993). Extending these early works, we perform retrospectively a more exhaustive analysis of AERONET data at four stations in the USA and Brazil (GSFC, Sevilleta, Cuiaba and Brasilia) to evaluate Pinatubo aerosol size evolution in 1993–1994 (Fig. 8c). We overlay our results with the synthesis of Russell et al. (1996) (Fig. 8d).

The short temporal overlap between Russell et al. (1996) and our results at +2 years after eruption shows an agreement on Pinatubo aerosol radius ($\sim$0.5 μm) (Fig. 8c). In addition, the decreasing trend in Pinatubo aerosol size visible in our AERONET analysis for 1993-1995 is consistent with the time evolution of Pinatubo radius over the period 1991-1993 by Russell et al. (1996) (Fig. 8d). As a side remark, this agreement also implies that, within the scope of our analysis, AERONET-derived peak radius r_{peak} can be compared, in good approximation, with the effective radius derived from other techniques, such as in-situ measurements.

First-order conclusions can be raised from this comparison regarding the early aerosol growth rate and the year-long evolution of stratospheric aerosols. First, the timescale of stratospheric aerosol growth appears much longer following the June 1991 Pinatubo eruption compared to the HT-HH case. According to Russell et al. (1996), r_{eff} grew from around 0.2–0.3 μm in late 1991, up to 0.5–0.6 μm over the timescale of one year (Fig. 8c). Hence, it took about 3–4 months for the Pinatubo aerosols to reach the size reached by HT-HH aerosols in just a couple of weeks (0.4 μm).

Fast growth rate of HT-HH sulfate aerosols could be linked to the strong water component of the plume resulting from exceptionally powerful water-magma interactions during the eruption, which was comparatively limited during the 1991 Pinatubo eruption. This massive release of water is attested by satellite observations of an exceptional hydration of the stratosphere (Millan et al., 2022; Vömel et al., 2022). This input of water is expected to increase the level of hydroxyl OH-radicals, leading to faster oxidation of SO_2 (Pinto et al., 1989; Bekki, 1995; Zhu et al., 2022). Then, in the accumulation mode (>0.1 μm), aerosols grow by coagulation and by condensation of vapor onto existing particles (Seinfeld & Pandis, 2012; Kremser et al., 2016). Overall, the presence of excess water may have enhanced the positive feedback between an early formation of sulfuric acid, coagulation and condensation, leading to a faster aerosol growth rate of HT-HH aerosols.

Model simulations with large stratospheric water vapour input, compared to simulations that do not account for a large water abundance, show that the HT-HH SO_2 lifetime is halved, down to 12 days (Zhu et al., 2022). This timescale is comparable with our observed stabilization of aerosol radius during the first circumnavigation. Likewise, model simulations show an increase in r_{eff}, ranging from 0.2 to 0.35 μm or more, early February 2022, at 36 hPa ($\approx$ 21 km) (Zhu et al., 2022), a size consistent with our observations.

Apart from the available sulfur dioxide and water vapour budgets, the altitude of a volcanic plume is another important factor controlling the growth rate of aerosols (Bauman et al., 2003; Ansmann et al., 1997; Sioris et al., 2010). Besides, the massive release of water by the HT-HH eruption had specific effects on the dynamics of the plume that could, in turn, influence the evolution of the physico-chemical environment of these aerosols. For instance, both aerosols and water vapour descended together by 4 to 6 km until early February 2022 due to the cooling effect of water vapour, and then separated vertically as aerosols sedimented and water vapour ascended (Sellitto et al., 2022; Schoeberl et al., 2022; Legras et al., 2022). The initial cooling and descent have likely played a role in the accelerated formation of the sulfates.

A second conclusion concerns the size of the aerosols after the growth phase. In spite of a slower growth compared to HT-HH, our comparison shows that Pinatubo aerosols grew steadily over the course of about one year until reaching their maximum size of $\sim$ 0.5–0.6 μm. Hence, from + 4 months after eruption, Pinatubo aerosols are larger that HT-HH aerosols, until at least +1.3 year post-eruption (at the time of writing) (Fig. 8d). For Pinatubo, after reaching their maximum size, aerosol size started to decrease (Russell et al., 1996). In the 1993-1995 interval of time (+2-3 yrs after eruption), our analysis of AERONET observations indicates that Pinatubo particle peak radius further decrease from $\sim$ 0.50 down to $\sim$ 0.35 μm. This systematic decrease in aerosol size likely results from sedimentation of the fraction of larger particles in the population, whose signature had previously been outweighted by aerosol condensation and coagulation (Russell et al., 1996). In constrast, for HT-HH, we note that, after a transient homogeneization phase lasting $\sim$ 4 months, the amplitude of the HT-HH volcanic mode in VSDs remains relatively stable and homogeneous over the southern hemisphere (Fig. 8a). Coevally, the aerosol size does not show any clear, systematic and monotonous decay (at the time of writing) (Fig. 8b). This observation does not appear to match a scenario involving a fast decay of HT-HH aerosols. Nevertheless, despite being smaller than Pinatubo sulfate aerosols, HT-HH particles are still larger than for other recent stratospheric eruptions such as 2009 Sarychev (Kuril Islands) and 2008 Kasatochi (Aleutian Islands), with r_{eff} ranging in 0.15–0.30 μm in the three months post-eruption from balloon-borne experiments (Jégou et al., 2013) and sunphotometric observations at polar stations (N. T. O'Neill et al., 2012). An even smaller effective radius of 0.16 μm is reported for 2008 Kasatochi aerosols one month post-eruption from LIDAR observations (Hoffmann et al., 2010). The consequences of these contrasting aerosol microphysical behaviours on climate need to be examined.

5 Conclusions and perspectives

Uncertainty on the size distribution of stratospheric sulfate aerosols, a fundamental parameter for modeling the climate response to eruptions, affects modeled aerosol optical depth and lifetime of stratospheric aerosols (Haywood et al., 2010; Kravitz et al., 2011; Dhomse et al., 2014; Lurton et al., 2018), and may explain inaccurate evaluation of the volcanic forcing and the mismatch between simulated and observed temperature anomalies (Timmreck et al., 2010; Mann et al., 2015; Kremser et al., 2016). Narrowing down these uncertainties is essen-

tial to better predict the formation and growth of HT-HH sulfate aerosols, especially given the excess stratospheric water vapour conditions that prevailed after the Hunga Tonga eruption (Zhu et al., 2022). Furthermore, water vapour also has a radiative effect on its own, that may produce a slightly positive net warming of the atmosphere, hence opposite to the expected effect of sulfate aerosols alone (Sellitto et al., 2022; Jenkins et al., 2023). On the other hand, failing to account for sulfate aerosols in chemistry-climate model simulations would lead to a weakened polar vortex and an enhanced Brewer-Dobson Circulation (Wang et al., 2022). Accordingly, since the forcings from both sulfate aerosols and water components need to be jointly considered (Wang et al., 2022; Zhu et al., 2022), constraining aerosol size is essential to assess the net effect of the eruption on planetary radiative balance.

Contrary to spaceborne occultation/limb-scattering measurements (Wrana et al., 2021; Thomason et al., 2021; Taha et al., 2021; Khaykin et al., 2022), AERONET inversions present the advantage of not requiring any a priori assumption on particle size distribution or chemical composition for the retrieval of volume size distribution. Together with satellite observations, exhaustive analysis of photometric observations from the AERONET network allows us to track the size of HT-HH sulfate aerosols with time. Despite a remarkably rapid growth rate in the week after eruption, we show that HT-HH sulfate particles remain smaller than Pinatubo aerosols 1.3 years after eruption. For a fixed mass, smaller-size stratospheric aerosols have a greater climate impact than larger aerosols. Smaller particles scatter visible light more efficiently and will sediment at lower rate, implying a larger and longer-lasting tropospheric cooling (Pinto et al., 1989; Bauman et al., 2003; Timmreck et al., 2009; Kremser et al., 2016). Furthermore, ozone destruction is enhanced by smaller aerosols via heterogeneous stratospheric chemistry (Solomon, 1999; Tilmes et al., 2008) and chemistry-climate model simulations have already shown that HT-HH aerosols would enhance polar ozone loss (Wang et al., 2022). The cause of the peculiar microphysical properties of HT-HH aerosols might be traced back to strong magma-water interactions during the eruption. Yet, geological markers of pre-historical underwater eruptions are difficult to identify and their climate impact may have been overlooked.

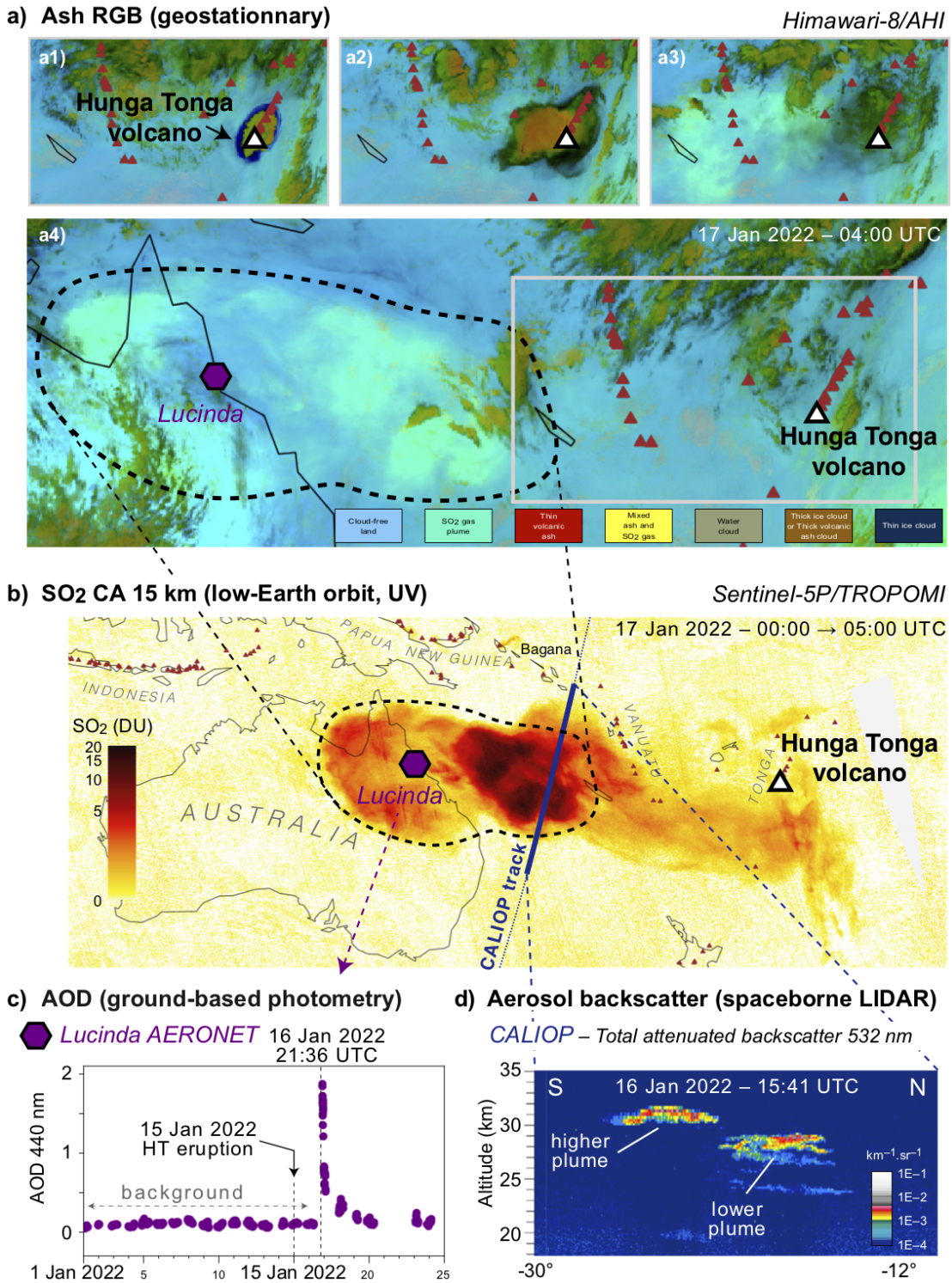

Figure 1. (a) Ash RGB products from HIMAWARI-8/AHI satellite observations of the near-source HT-HH plume from 15 January 2022 05:00 UTC to the time of TROPOMI acquisition detecting the dispersed plume over Australia (17 January 2022, 04:00 UTC). Grey rectangle in a4 shows extent of panels a1 to a3. Black triangle shows location of HT-HH volcano. Red triangles are other active volcanoes. (b) SO_2-rich plume from TROPOMI (15 km product) on 17 January (between 00:00 and 05:00 UTC) with indication of the track of CALIOP spaceborne LIDAR night-time observations (dark blue line) crossing the plume ≈10 hours before TROPOMI acquisition, and of the location of the AERONET ground station of Lucinda in eastern Australia (white square). (c) AOD_{440nm} L1.5 values observed at Lucinda in January 2022 until the arrival of HT-HH aerosols on 16 January 2022. (d) Total attenuated backscatter signal (at 532 nm) with altitude along the portion of the CALIOP track detecting HT-HH aerosols (16 January 2022, 15:41 UTC, latitudes ranging in -30° to -12°).

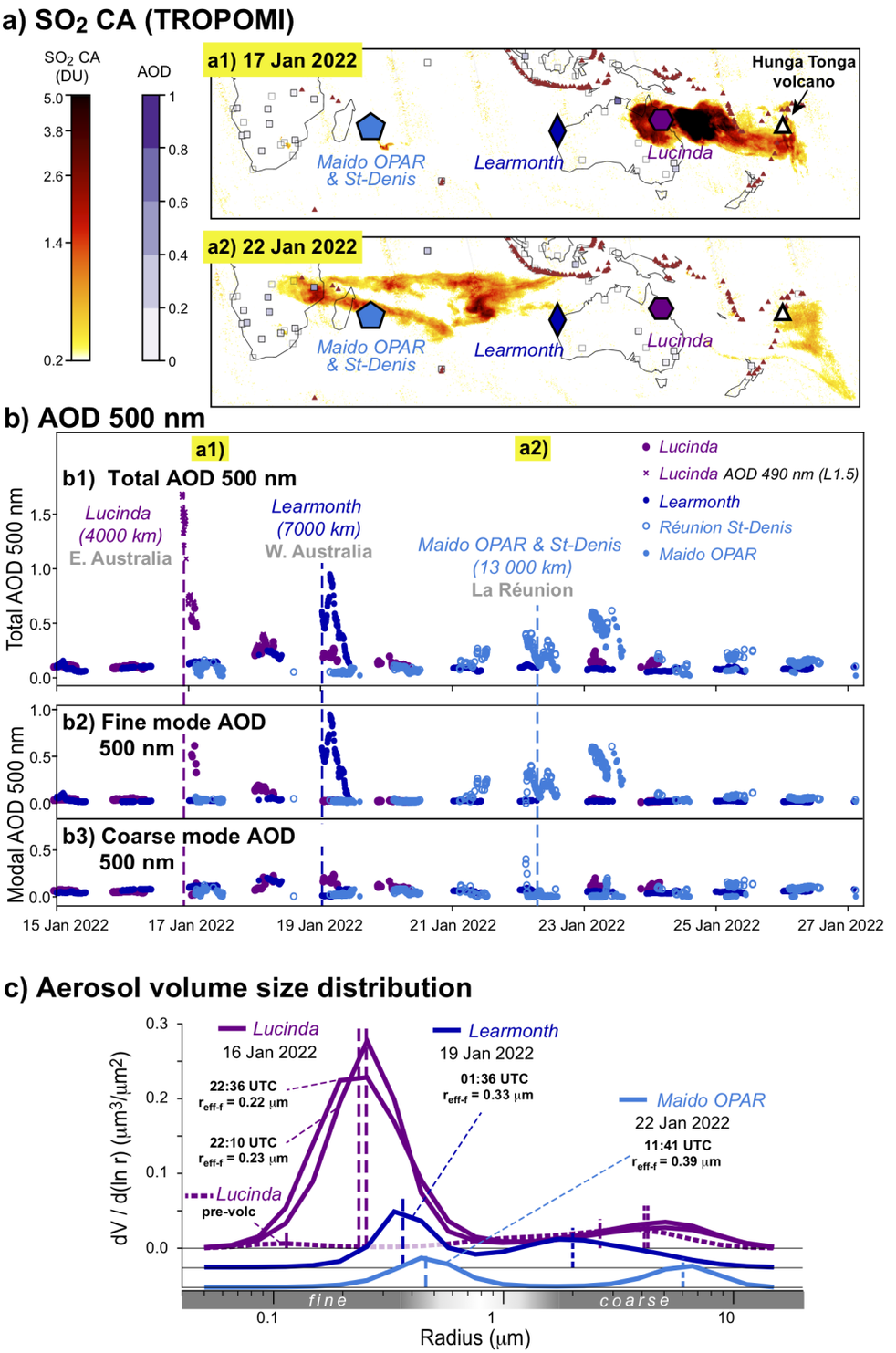

Figure 2. (a) HT-HH SO_2-rich plume from Sentinel-5P/TROPOMI column amount observations (15 km product) on (a1) 17 and (a2) 22 January 2022, with indication of the AERONET stations (squares colored according to daily mean AOD_{440nm}) of Lucinda (eastern Australia, purple), Learmonth (western Australia, dark blue), Maido OPAR (sky blue, solid circles) and St-Denis (sky blue, circles) (both on Réunion Island), respectively at 4000, 7000 and 13000 km from the volcanic source. (b) Time series of (b1) total, (b2) fine and (b3) coarse mode AOD_{500nm} (SDA algorithm) from L1.5 direct sun observations (circles). Note that the plot is complemented with L1.5 total AOD observations at 490 nm (crosses) for Lucinda, which provide a better temporal coverage. (c) Aerosol volume size distribution derived from almucantar observations (date indicated by vertical dashed lines in (b)) first available after the arrival of the HT-HH plume at the stations (vertical dashed lines indicate r_{peak} in both fine/coarse modes).

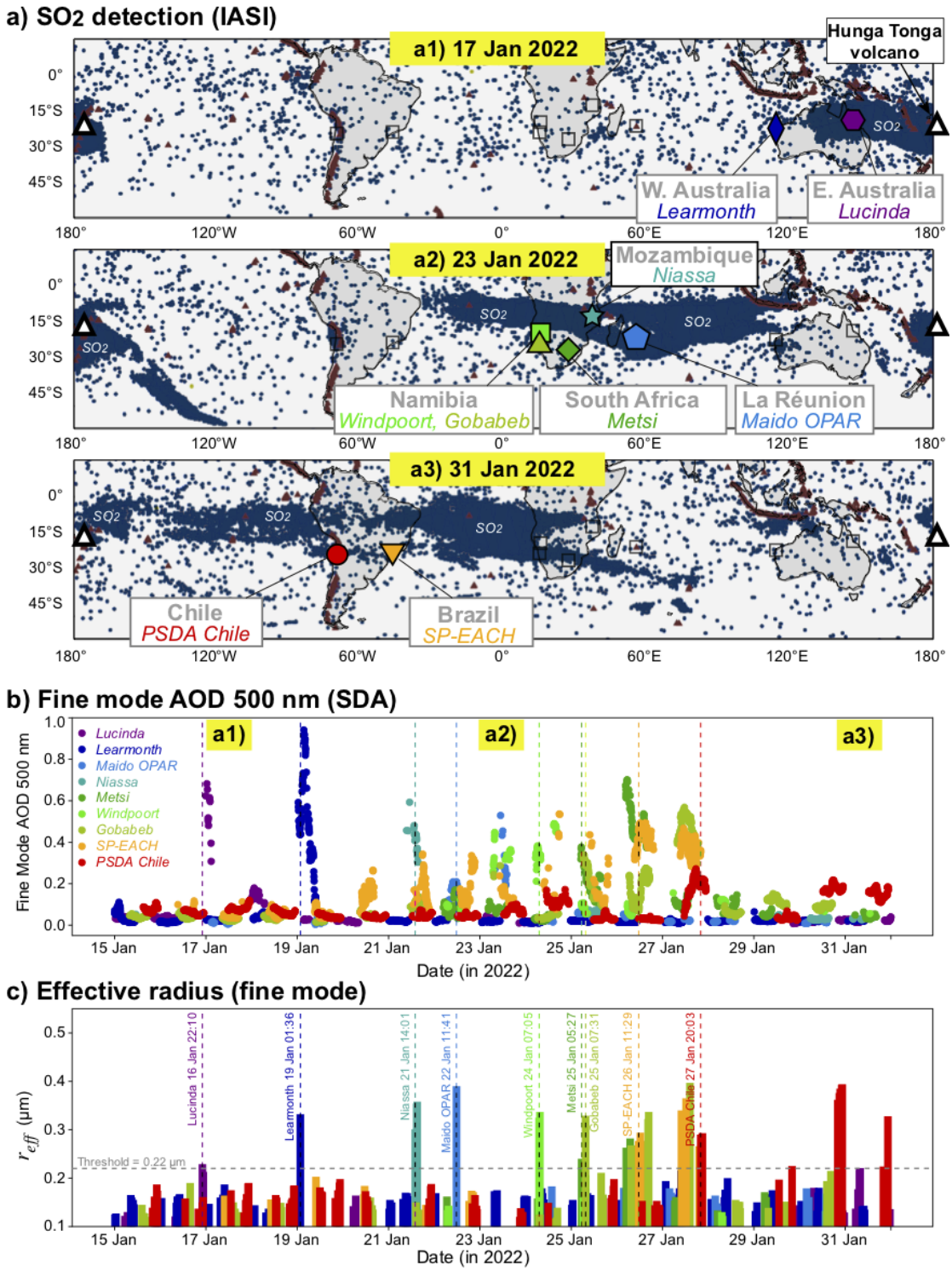

Figure 3. (a) Transport and dispersion of the HT-HH SO_2 plume during first circumnavigation around the globe. Blue dots show SO_2 detection from MetOp-B and -C/IASI AM and PM observations, retrieved from SO_2 height products, on (a1) 17, (a2) 23 and (a3) 31 January 2022. Symbols indicate the location of ground-based AERONET photometric observations displayed in (b) and (c) with colors varying with longitude. (b) Fine mode $AOD_{500\,nm}$ (SDA algorithm) from direct sun measurements. (c) Fine mode effective radius from almucantar observations. Vertical dashed lines indicate, for each of the stations, the time of first detection of HT-HH aerosols (defined as particles with a fine mode $r_{eff} > 0.22$ μm.)

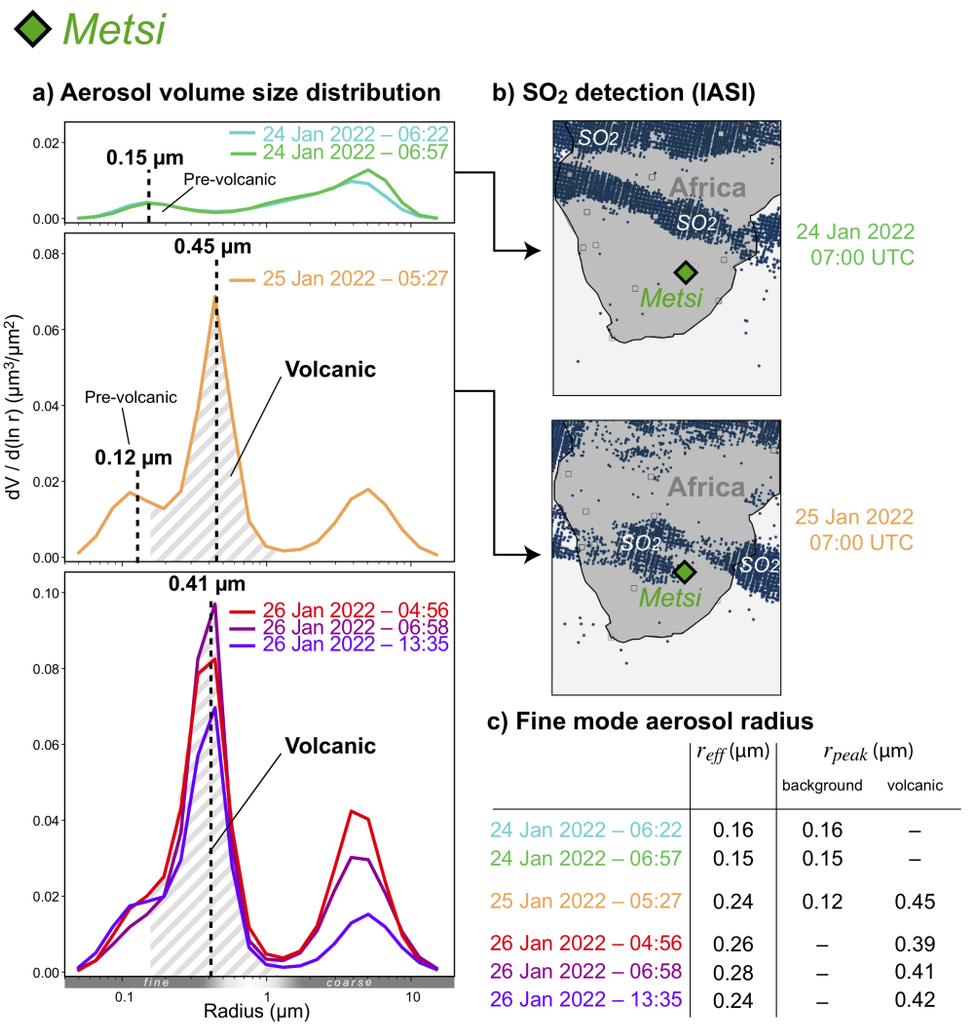

c) Fine mode aerosol radius

	r_{eff} (µm)	r_{peak} (µm)	
		background	volcanic
24 Jan 2022 – 06:22	0.16	0.16	–
24 Jan 2022 – 06:57	0.15	0.15	–
25 Jan 2022 – 05:27	0.24	0.12	0.45
26 Jan 2022 – 04:56	0.26	–	0.39
26 Jan 2022 – 06:58	0.28	–	0.41
26 Jan 2022 – 13:35	0.24	–	0.42

Figure 4. Detection of volcanic aerosols at Metsi AERONET station (South Africa) at the time of first overpass by the HT-HH plume. (a) Aerosol VSD on (top) 24 January 2022 (background or pre-volcanic), (middle) 25 and (bottom) 26 January 2022 (impacted by HT-HH), with indication in bold of radii (r_{peak}) of local maxima of the VSD identified with a spline interpolation. (b) Detection of the HT-HH SO_2 plume using MetOp-B and -C/IASI SO_2 height product on (top) 24 and (bottom) 25 January AM ($\sim$ 07:00 UTC) with the location of Metsi station indicated by a green diamond. (c) Table of AERONET-derived particle size in the fine range (μm): fine mode effective radius (r_{eff}, left) and peak radius (r_{peak}, right). For r_{peak}, background and volcanic aerosol radii may be estimated simultaneously, and are distinguished in two separate columns.

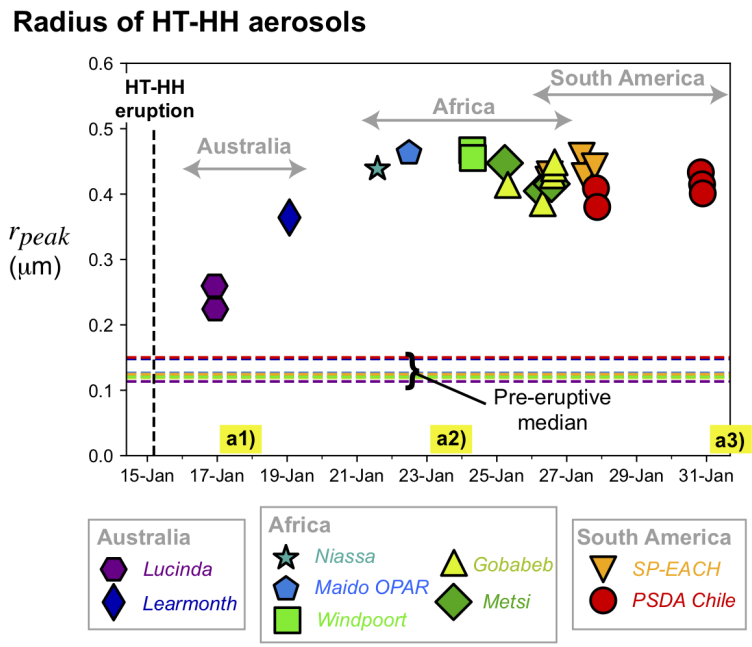

Figure 5. HT-HH aerosol peak radius during first circumnavigation of the globe (January 2022), at selected AERONET stations in three different continents indicated by colored symbols (AOD_{440nm}>0.1). This size corresponds to the radius of the aerosols giving the largest contribution to the volume size distribution in the fine range ($r_{peak,1}$). Horizontal dashed lines indicate the median of $r_{peak,1}$ in the fine mode between 1 January 2020 and 15 January 2022 (date of the eruption) for each station. Vertical dashed line marks the time of the HT-HH eruption. Annotations (a1) 17 Jan, (a2) 23 Jan and (a3) 31 Jan 2022 refer to the time of IASI SO_2 detections in Fig. 3. VSDs associated to each datapoint are shown in Fig. S5.

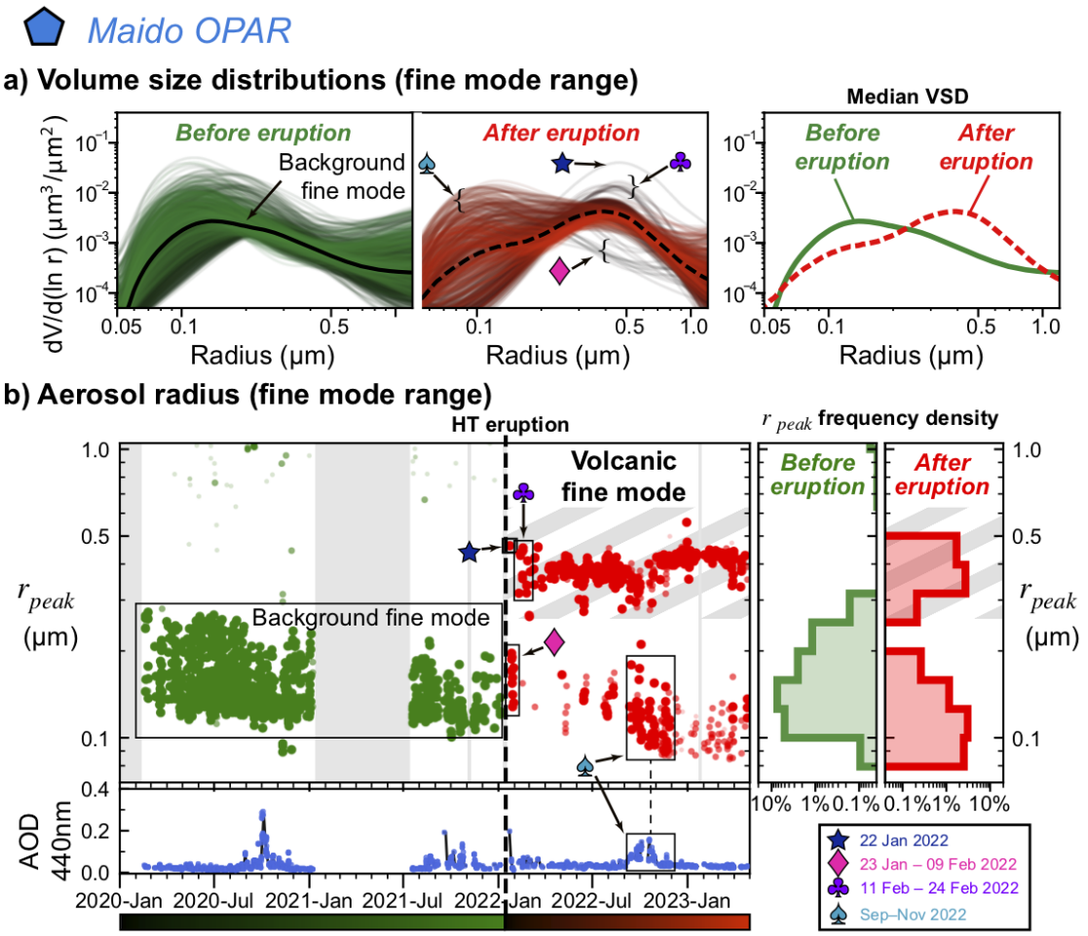

Figure 6. Aerosol size over La Réunion island/Maido OPAR station (21°S) from January 2020 to May 2023. (a) VSDs displayed in the fine mode range before (left, green) and after (middle, red) the HT-HH eruption, for the subset of VSDs with $r_{peak,1}$<0.90 μm or $r_{peak,2}$<0.90 μm (ie. those including either their largest or second-largest peak in the fine mode range). Color coding varies with time, as indicated by the colorscale at the bottom of the figure. Thick black lines show the median of the VSDs, which are duplicated in the right panel to facilitate comparison. (b) Aerosol peak radius in the fine mode range. Eruption date is indicated by a vertical dashed line. Left panel: time series of radii $r_{peak,i}$ associated to local maxima in the spline interpolation of the aerosol VSD. The three largest local maxima ($r_{peak,i}$, with i=1,2,3) are ordered from largest to lowest volume abundances and displayed with symbols of decreasing size and opacity. Grey areas indicate data gaps longer than 15 days. Right panel: frequency density histograms of r_{peak} before/after eruption. Symbols highlight detections of special interest, discussed in the text (★: first plume overpass on 22 Jan 2022; ♦: temporary lull during first circumnavigation; ♣: resumption of the volcanic signal during second overpass and continued detection thereafter; ♠: increased background fine mode due to biomass burning). The full distribution of r_{peak}, including the coarse mode range, is illustrated in Fig. S8b.

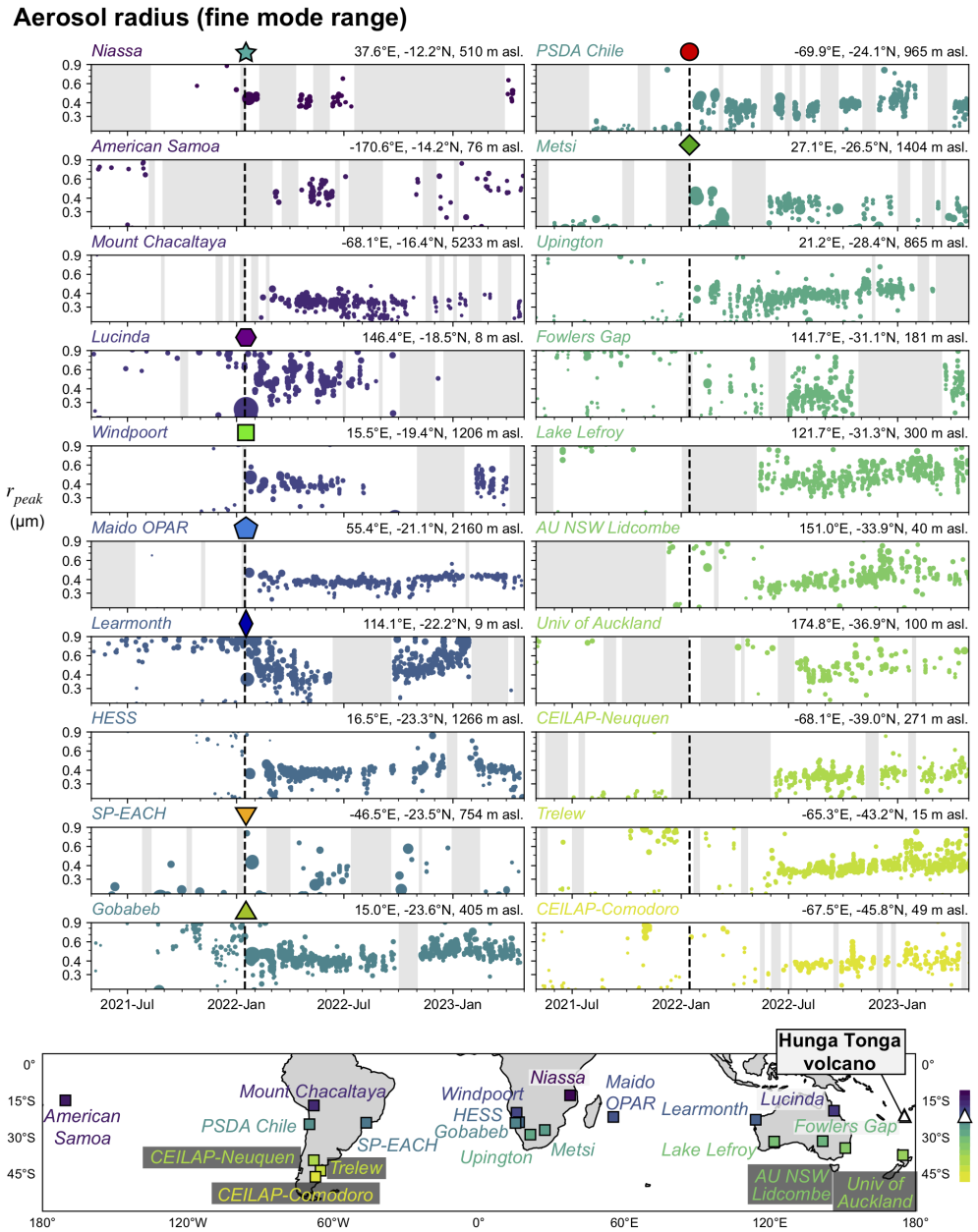

Figure 7. Aerosol peak radius r_{peak} associated to the HT-HH volcanic fine mode (plotted in the 0.22-0.90 μm range), from May 2021 to May 2023, at 20 AERONET stations of the southern hemisphere. To avoid clutter, only the largest and second-largest peaks of each VSD are plotted (ie., $r_{peak,1}$ and $r_{peak,2}$), with symbol size proportional to VSD amplitude at the peak (ie., $A_{peak,1}$ and $A_{peak,2}$, respectively). The color of station symbol varies with latitude, as shown in the map in the bottom panel. Grey areas indicate data gaps longer than 15 days. Aerosol r_{peak} values covering the whole size range (fine and coarse modes) are illustrated for each station in Fig. S7 to S9. HT-HH eruption is indicated by dashed vertical line. The symbols of the nine stations discussed in Section 3.1.2 are recalled at the top of each sub-panel.

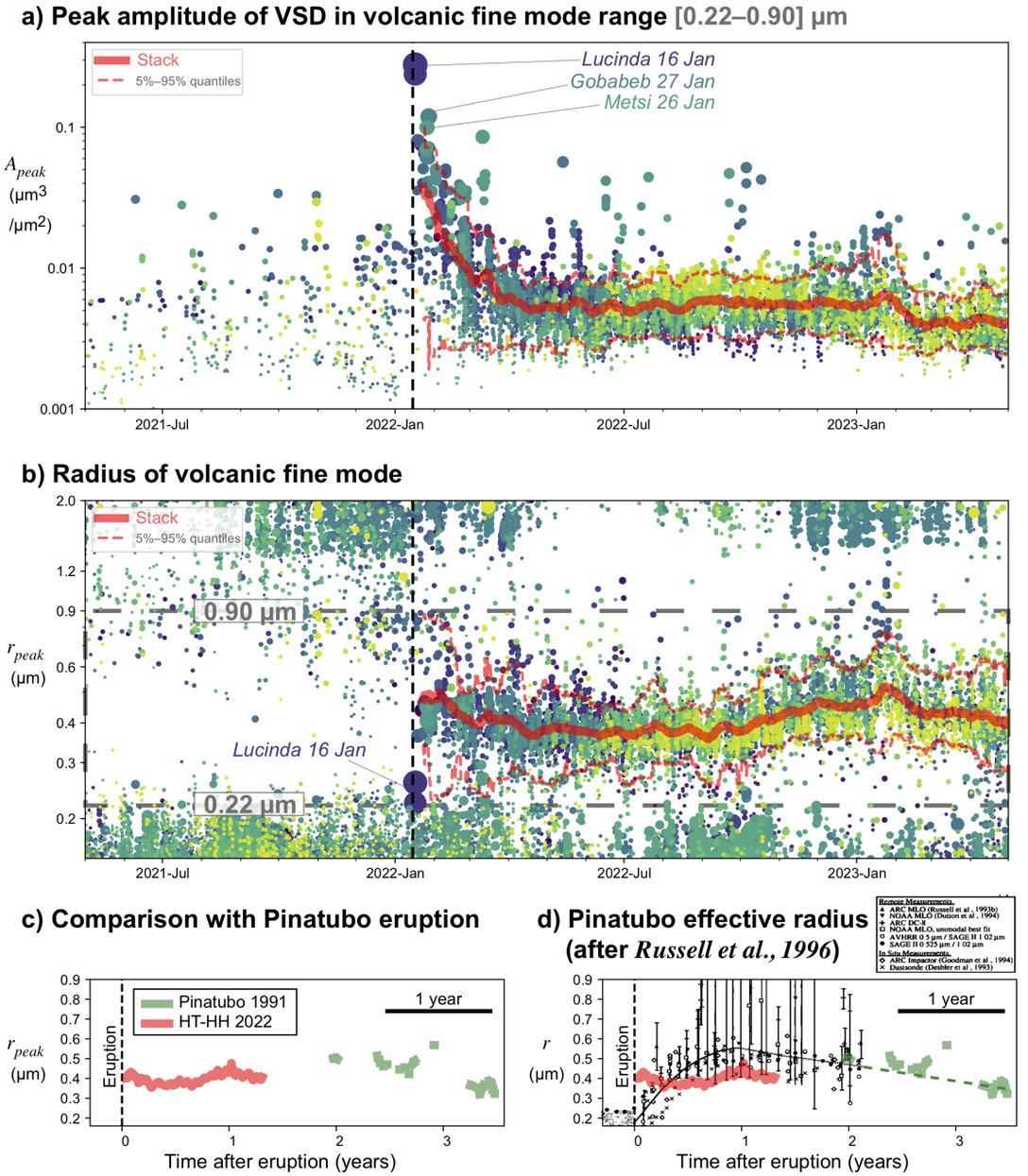

Figure 8. (a) Stack of the time-series of aerosol peak amplitudes A_{peak} for the largest and second-largest peaks situated within the volcanic size range (ie., $A_{peak,1}$, if $r_{peak,1} \in [0.22 - 0.90]$ μm, and $A_{peak,2}$, if $r_{peak,2} \in [0.22 - 0.90]$ μm) at the 20 stations of the southern hemisphere shown in Fig. 7. (b) Stack of the time-series of aerosol peak radius $r_{peak,i}$ (with i=1,2). In (a) and (b), the thick red line is the rolling median computed after the HT-HH eruption (vertical dashed line) with a window size of 15 days, restricted to data points falling within the volcanic size range. Dashed red lines are the 5% and 95% quantiles. Symbol size is proportional to A_{peak}, while colors depend on station latitude, as in Fig. 7. (c) Temporal evolution of aerosol radius based on the analysis of AERONET data for HT-HH (red, same as in (b)) and Pinatubo (green) until + 1300 days post-eruption. The analysis of AERONET data for Pinatubo 1991 was conducted using the same methodology as for HT-HH, albeit with a more limited dataset (first data point: mid-1993). See Figure S12 for details of the analysis of the Pinatubo 1991 particles. (d) Same as (c), overlaid on the effective radius of Pinatubo aerosols from Fig. 4 in the compilation by Russell et al. (1996), filling the gap of AERONET data in the 1991–1993 interval. Green dashed line is the prolongation of the mid-1992-to-mid-1993 trend of Russell et al. (1996).

Open Research Section

All data used in this study are publicly available:

- Facilities of the European Space Agency (ESA) were used for access to Sentinel-5P TROPOMI Level 2 SO2 products (ESA Copernicus, 2020)
- Facilities of EUMETSAT SAF on Atmospheric Composition Monitoring (`http://ac-saf.eumetsat.int`) were used for access to MetOp-B and MetOp-C/IASI L2 column amount products (EUMETSAT, 2018)
- The IASI portal of the AERIS Data and Services Center (`https://iasi.aeris-data.fr`) was used for access to MetOp-B and MetOp-C IASI L2 columns and altitude products (Clarisse, 2013, 2019)
- The Data Integration and Analysis System (DIAS) by Japan Agency for Marine-Earth Science and Technology (JAMSTEC) was used for access to Himawari-8 Level 1B products (Japan Meteorological Agency, 2015)
- Facilities of NASA-LARC (`https://www-calipso.larc.nasa.gov/`) were used for access to CALIPSO-CALIOP Level 1B products (NASA/CNES/LARC/SD/ASDC, 2022)
- Facilities of NASA-GSFC (`https://aeronet.gsfc.nasa.gov/cgi-bin/webtool_inv_v3`) were used for access to AERONET Level 1.5 products (AERONET Federation, 1993)

The VOLCPLUME web-based portal, freely, accessible via `https://volcplume.aeris-data.fr`, and hosted by AERIS/ICARE Data and Services Center (`https://www.icare.univ-lille.fr/data-policy/?policy=icare`) was used for satellite and ground-based multi-station analysis (Boichu & Mathurin, 2022).

Acknowledgments

Support from AERIS/ICARE Data and Services centre, for the co-development of the VOLCPLUME web portal (`https://doi.org/10.25326/362`), and Horizon Europe FAIR-EASE project (grant No. 101058785) are acknowledged. This work is a contribution to the CaPPA project (ANR-11-LABX-0005-01) funded by ANR, Hauts-de-France Region and FEDER. AERONET staff is thanked for calibrating and maintaining instrumentation of the network as well as data processing. We warmly thank the site managers: V. Duflot (Maido OPAR, Réunion St-Denis), T. Schroeder (Lucinda), I. Lau (Learmonth), A. Queface (Niassa), P. Gupta (Metsi), K. Negussie (Windpoort), S. Piketh (Gobabeb), A. Marzo (PSDA Chile) and M. Yamasoe (SP-EACH). We acknowledge the French component of AERONET operating within the Center for Aerosol Remote sensing (CARS) of the ACTRIS Atmospheric Research Infrastructure.

We thank four anonymous reviewers for their insightful comments.

References

AERONET Federation. (1993). *AErosol RObotic NETwork (AERONET) Level 1.5 aerosol products, V3* [Dataset]. Retrieved from `https://aeronet.gsfc.nasa.gov/new_web/data_description.html`

Ansmann, A., Mattis, I., Wandinger, U., Wagner, F., Reichardt, J., & Deshler, T. (1997). Evolution of the Pinatubo aerosol: Raman lidar observations of particle optical depth, effective radius, mass, and surface area over Central Europe at 53.4 N. *Jour-*

nal of the atmospheric sciences, *54*(22), 2630–2641.

Asano, S., Uchiyama, A., & Shiobara, M. (1993). NOTES AND CORRESPONDENCE: Spectral Optical Thickness and Size Distribution of the Pinatubo Volcanic Aerosols as Estimated by Ground-Based Sunphotometry. *Journal of the Meteorological Society of Japan. Ser. II*, *71*(1), 165–173.

Baron, A., Chazette, P., Khaykin, S., Payen, G., Marquestaut, N., Bègue, N., & Duflot, V. (2023). Early Evolution of the Stratospheric Aerosol Plume Following the 2022 Hunga Tonga-Hunga Ha'apai Eruption: Lidar Observations From Reunion (21° S, 55° E). *Geophysical Research Letters*, *50*(10), e2022GL101751.

Barreto, Á., A.E., C., Granados-Muñoz, M., Alados-Arboledas, L., Romero Campos, P., Gröbner, J., ... others (2016). The new sun-sky-lunar Cimel CE318-T multiband photometer – a comprehensive performance evaluation. *Atmospheric Measurement Techniques*, *9*(2), 631–654.

Bauman, J., Russell, P., Geller, M., & Hamill, P. (2003). A stratospheric aerosol climatology from SAGE II and CLAES measurements: 2. Results and comparisons, 1984–1999. *Journal of Geophysical Research: Atmospheres*, *108*(D13).

Bekki, S. (1995). Oxidation of volcanic SO2: a sink for stratospheric OH and H2O. *Geophysical Research Letters*, *22*(8), 913–916.

Bluth, G. J., Doiron, S. D., Schnetzler, C. C., Krueger, A. J., & Walter, L. S. (1992). Global tracking of the SO2 clouds from the June, 1991 Mount Pinatubo eruptions. *Geophysical Research Letters*, *19*(2), 151–154.

Boichu, M., & Mathurin, T. (2022). *VOLCPLUME, an interactive web portal for the multiscale analysis of volcanic plume physico-chemical properties* [Interactive Web-based Ressource]. Direct access: https://volcplume.aeris-data.fr. Retrieved August 2023, from `https://www.icare.univ-lille.fr/volcplume/` doi: 10.25326/362

Bourassa, A. E., Zawada, D. J., Rieger, L. A., Warnock, T. W., Toohey, M., & Degenstein, D. A. (2023). Tomographic Retrievals of Hunga Tonga-Hunga Ha'apai Volcanic Aerosol. *Geophysical Research Letters*, *50*(3), e2022GL101978.

Carn, S., Krotkov, N., Fisher, B., & Li, C. (2022). Out of the blue: Volcanic SO2 emissions during the 2021–2022 eruptions of Hunga Tonga—Hunga Ha'apai (Tonga). *Frontiers in Earth Science*, *10*, 976962.

Carr, J. L., Horváth, Á., Wu, D. L., & Friberg, M. D. (2022). Stereo Plume Height and Motion Retrievals for the Record-Setting Hunga Tonga-Hunga Ha'apai Eruption of 15 January 2022. *Geophysical Research Letters*, *49*(9), e2022GL098131.

Clain, G., Baray, J.-L., Delmas, R., Diab, R., Leclair de Bellevue, J., Keckhut, P., ... Cammas, J.-P. (2009). Tropospheric ozone climatology at two Southern Hemisphere tropical/subtropical sites, (Reunion Island and Irene, South Africa) from ozonesondes, LIDAR, and in situ aircraft measurements. *Atmospheric Chemistry and Physics*, *9*(5), 1723–1734.

Clarisse, L. (2013). *MetOp-B IASI Level 2 Sulphur Dioxide Total Column and Altitude. V2.1.0* [Dataset]. Retrieved from `https://www.aeris-data.fr/en/landing-page/?uuid=72b08c4b-cf05-4bd7-ae16-4c0dd2a889c3` doi: 10.25326/42

Clarisse, L. (2019). *MetOp-C IASI Level 2 Sulphur Dioxide Total Column and Altitude. V2.1.0* [Dataset]. Retrieved from `https://www.aeris-data.fr/en/landing-page/?uuid=3e81c051-cc66-4a81-a5e5-48cedcd53dfb` doi: 10.25326/43

Clarisse, L., Coheur, P.-F., Theys, N., Hurtmans, D., & Clerbaux, C. (2014). The 2011 Nabro eruption, a SO_2 plume height analysis using IASI measurements. *Atmos. Chem. Phys.*, *14*(6), 3095–3111.

Coy, L., Newman, P., Wargan, K., Partyka, G., Strahan, S., & Pawson, S. (2022). Strato-

spheric Circulation Changes Associated with the Hunga Tonga-Hunga Ha'apai Eruption. *Geophysical Research Letters*, e2022GL100982.

Deshler, T. (2008). A review of global stratospheric aerosol: Measurements, importance, life cycle, and local stratospheric aerosol. *Atmospheric Research*, *90*(2-4), 223–232.

Dhomse, S., Emmerson, K., Mann, G., Bellouin, N., Carslaw, K., Chipperfield, M., ... others (2014). Aerosol microphysics simulations of the Mt. Pinatubo eruption with the UM-UKCA composition-climate model. *Atmospheric Chemistry and Physics*, *14*(20), 11221–11246.

Dubovik, O., Holben, B., Eck, T. F., Smirnov, A., Kaufman, Y. J., King, M. D., ... Slutsker, I. (2002). Variability of absorption and optical properties of key aerosol types observed in worldwide locations. *Journal of the Atmospheric Sciences*, *59*(3), 590–608.

Dubovik, O., & King, M. D. (2000). A flexible inversion algorithm for retrieval of aerosol optical properties from sun and sky radiance measurements. *Journal of Geophysical Research: Atmospheres*, *105*(D16), 20673–20696.

Dubovik, O., Sinyuk, A., Lapyonok, T., Holben, B. N., Mishchenko, M., Yang, P., ... Slutsker, I. (2006). Application of spheroid models to account for aerosol particle nonsphericity in remote sensing of desert dust. *J. Geophys. Res. Atm.*, *111*(D11208).

Dubovik, O., Smirnov, A., Holben, B., King, M., Kaufman, Y., Eck, T., & Slutsker, I. (2000). Accuracy assessments of aerosol optical properties retrieved from Aerosol Robotic Network (AERONET) Sun and sky radiance measurements. *Journal of Geophysical Research: Atmospheres*, *105*(D8), 9791–9806.

Duchamp, C., Wrana, F., Legras, B., Sellitto, P., Belhadji, R., & von Savigny, C. (2023). Observation of the aerosol plume from the 2022 Hunga Tonga-Hunga Ha'apai eruption with SAGE III/ISS. *Authorea Preprints*. Retrieved August 2023, from `https://www.doi.org/10.22541/essoar.168771425.59096731/v1` doi: 10.22541/essoar.168771425.59096731/v1

Eck, T., Holben, B., Reid, J., Dubovik, O., Smirnov, A., O'neill, N., ... Kinne, S. (1999). Wavelength dependence of the optical depth of biomass burning, urban, and desert dust aerosols. *Journal of Geophysical Research: Atmospheres*, *104*(D24), 31333–31349.

Eck, T. F., Holben, B. N., Sinyuk, A., Pinker, R., Goloub, P., Chen, H., ... others (2010). Climatological aspects of the optical properties of fine/coarse mode aerosol mixtures. *Journal of Geophysical Research: Atmospheres*, *115*(D19).

ESA Copernicus. (2020). *Sentinel-5P TROPOMI Level 2 Sulphur Dioxide Total Column. Version 02.* [Dataset]. Retrieved from `https://scihub.copernicus.eu/` doi: 10.5270/S5P-74eidii

EUMETRAIN. (2023). *SEVIRI ash RGB Quick Guide.* Retrieved from `https://resources.eumetrain.org/rgb_quick_guides/index.html`

EUMETSAT. (2018). *MetOp IASI Level 2 Sulphur Dioxide Total Column* [Dataset]. Retrieved from `https://navigator.eumetsat.int/product/EO:EUM:DAT:METOP:MXI-N-SO2`

EUMETSAT. (2023). *Compilation of RGB recipes.* Retrieved January 2023, from `https://eumetrain.org/sites/default/files/2022-10/RGB_recipes.pdf`

Folch, A., Costa, A., Durant, A., & Macedonio, G. (2010). A model for wet aggregation of ash particles in volcanic plumes and clouds: 2. Model application. *Journal of Geophysical Research (Solid Earth)*, *115*(B14), 9202. doi: 10.1029/2009JB007176

Foucart, B., Sellegri, K., Tulet, P., Rose, C., Metzger, J.-M., & Picard, D. (2018). High

occurrence of new particle formation events at the Maïdo high-altitude observatory (2150 m), Réunion (Indian Ocean). *Atmospheric Chemistry and Physics*, *18*(13), 9243–9261.

Giles, D. M., Sinyuk, A., Sorokin, M. G., Schafer, J. S., Smirnov, A., Slutsker, I., ... others (2019). Advancements in the Aerosol Robotic Network (AERONET) Version 3 database–automated near-real-time quality control algorithm with improved cloud screening for Sun photometer aerosol optical depth (AOD) measurements. *Atmospheric Measurement Techniques*, *12*(1), 169–209.

Haywood, J. M., Jones, A., Clarisse, L., Bourassa, A., Barnes, J., Telford, P., ... Braesicke, P. (2010). Observations of the eruption of the Sarychev volcano and simulations using the HadGEM2 climate model. *J. Geophys. Res.*, *115*, D21212. doi: 10.1029/2010JD014447

Hoffmann, A., Ritter, C., Stock, M., Maturilli, M., Eckhardt, S., Herber, A., & Neuber, R. (2010). Lidar measurements of the Kasatochi aerosol plume in August and September 2008 in Ny-Ålesund, Spitsbergen. *Journal of Geophysical Research: Atmospheres*, *115*(D2).

Holben, B., Setzer, A., Eck, T., Pereira, A., & Slutsker, I. (1996). Effect of dry-season biomass burning on Amazon basin aerosol concentrations and optical properties, 1992–1994. *Journal of Geophysical Research: Atmospheres*, *101*(D14), 19465–19481.

Holben, B., Smirnov, A., Eck, T. F., Slutsker, I., Abuhassan, N., Newcomb, W. W., ... Lavenu, F. (2001). An emerging ground-based aerosol climatology- Aerosol optical depth from AERONET. *J. Geophys. Res.*, *106*(D11), 12067–12097.

Holben, B. N., Eck, T., Slutsker, I., Smirnov, A., Sinyuk, A., Schafer, J., ... Dubovik, O. (2006). Aeronet's version 2.0 quality assurance criteria. In *Remote sensing of the atmosphere and clouds* (Vol. 6408, pp. 134–147).

Holben, B. N., Eck, T. F., Slutsker, I., Tanré, D., Buis, J. P., Setzer, A., ... Smirnov, A. (1998). AERONET–A Federated Instrument Network and Data Archive for Aerosol Characterization. *Remote Sensing of Environment*, *66*(1), 1 - 16. doi: 10.1016/S0034-4257(98)00031-5

Japan Meteorological Agency. (2015). *Himawari 8, Advanced Himawari Imager (AHI), L1B* [Dataset]. Retrieved from `https://search.diasjp.net/en/dataset/Himawari_8_9`

Japan Meteorological Agency. (2023). *Himawari ash RGB quich guide.* Retrieved January 2023, from `https://www.jma.go.jp/jma/jma-eng/satellite/VLab/QG/RGB_QG_Ash_en.pdf`

Jégou, F., Berthet, G., Brogniez, C., Renard, J.-B., François, P., Haywood, J. M., ... Daugeron, D. (2013). Stratospheric aerosols from the Sarychev volcano eruption in the 2009 Arctic summer. *Atmospheric Chemistry and Physics*, *13*(13), 6533–6552. Retrieved from `http://www.atmos-chem-phys.net/13/6533/2013/` doi: 10.5194/acp-13-6533-2013

Jenkins, S., Smith, C., Allen, M., & Grainger, R. (2023). Tonga eruption increases chance of temporary surface temperature anomaly above 1.5 ° c. *Nature Climate Change*, 1–3.

Khaykin, S., Podglajen, A., Ploeger, F., Grooß, J.-U., Tencé, F., Bekki, S., ... others (2022). Global perturbation of stratospheric water and aerosol burden by Hunga eruption. *Communications Earth & Environment*, *3*(1), 316.

Kloss, C., Sellitto, P., Renard, J.-B., Baron, A., Bègue, N., Legras, B., ... others (2022). Aerosol characterization of the stratospheric plume from the volcanic

eruption at Hunga Tonga 15 January 2022. *Geophysical Research Letters*, *49*(16), e2022GL099394.

Koren, I., Dagan, G., & Altaratz, O. (2014). From aerosol-limited to invigoration of warm convective clouds. *science*, *344*(6188), 1143–1146.

Kravitz, B., Robock, A., Bourassa, A., Deshler, T., Wu, D., Mattis, I., ... others (2011). Simulation and observations of stratospheric aerosols from the 2009 Sarychev volcanic eruption. *Journal of Geophysical Research: Atmospheres*, *116*(D18).

Kremser, S., Thomason, L. W., von Hobe, M., Hermann, M., Deshler, T., Timmreck, C., ... others (2016). Stratospheric aerosol—observations, processes, and impact on climate. *Reviews of Geophysics*, *54*(2), 278–335.

Lac, C., Le Pichon, A., Listowski, C., Abbassi, G., Astafyeva, E., Baron, A., ... others (2022). *The eruption of the Hunga Tonga - Hunga Ha'apai volcano on January 15, 2022: a shock of the Earth on a global scale* (Tech. Rep.). Groupe Thématique Atmosphère d'ALLENVI. Retrieved Jan 2023, from `https://zenodo.org/record/7678770/files/Tonga_FR_FINALE_DOI_v1.1.pdf` doi: 10.5281/zenodo.7678770

Legras, B., Duchamp, C., Sellitto, P., Podglajen, A., Carboni, E., Siddans, R., ... Ploeger, F. (2022). The evolution and dynamics of the Hunga Tonga–Hunga Ha'apai sulfate aerosol plume in the stratosphere. *Atmospheric Chemistry and Physics*, *22*(22), 14957–14970.

Lurton, T., Jégou, F., Berthet, G., Renard, J.-B., Clarisse, L., Schmidt, A., ... Roberts, T. J. (2018). Model simulations of the chemical and aerosol microphysical evolution of the Sarychev Peak 2009 eruption cloud compared to in situ and satellite observations. *Atmospheric Chemistry and Physics*, *18*(5), 3223–3247.

Mann, G., Dhomse, S., Deshler, T., Timmreck, C., Schmidt, A., Neely, R., & Thomason, L. (2015). Evolving particle size is the key to improved volcanic forcings. *Past Global Changes Magazine*, *23*, 52–53.

Marshall, L. R., Maters, E. C., Schmidt, A., Timmreck, C., Robock, A., & Toohey, M. (2022). Volcanic effects on climate: recent advances and future avenues. *Bulletin of Volcanology*, *84*(5), 1–14.

McCormick, M. P., Thomason, L. W., & Trepte, C. R. (1995). Atmospheric effects of the Mt Pinatubo eruption. *Nature*, *373*, 399-404. doi: 10.1038/373399a0

Millan, L., Santee, M. L., Lambert, A., Livesey, N. J., Werner, F., Schwartz, M. J., ... others (2022). The Hunga Tonga-Hunga Ha'apai Hydration of the Stratosphere. *Geophysical Research Letters*, *49*(13), e2022GL099381.

NASA/CNES/LARC/SD/ASDC. (2022). *CALIPSO Lidar Level 1B profile data, V4.51* [Dataset]. doi: 10.5067/CALIOP/CALIPSO/CAL_LID_L1-Standard-V4-51

O'Neill, N., Eck, T., Smirnov, A., Holben, B., & Thulasiraman, S. (2003). Spectral discrimination of coarse and fine mode optical depth. *J. Geophys. Res. Atmos.*, *108*(D17).

O'Neill, N. T., Perro, C., Saha, A., Lesins, G., Duck, T. J., Eloranta, E. W., ... others (2012). Properties of Sarychev sulphate aerosols over the Arctic. *J. Geophys. Res.*, *117*(D4).

Pinto, J. P., Turco, R. P., & Toon, O. B. (1989). Self-limiting physical and chemical effects in volcanic eruption clouds. *Journal of Geophysical Research: Atmospheres*, *94*(D8), 11165–11174.

Prata, A. (1989). Infrared radiative transfer calculations for volcanic ash clouds. *Geophysical research letters*, *16*(11), 1293–1296.

Proud, S. R., Prata, A. T., & Schmauß, S. (2022). The January 2022 eruption of Hunga Tonga-Hunga Ha'apai volcano reached the mesosphere. *Science*, *378*(6619), 554–

557.

Randriambelo, T., Baray, J.-L., & Baldy, S. (2000). Effect of biomass burning, convective venting, and transport on tropospheric ozone over the indian ocean: Reunion island field observations. *Journal of Geophysical Research: Atmospheres*, *105*(D9), 11813–11832.

Ridley, D., Solomon, S., Barnes, J., Burlakov, V., Deshler, T., Dolgii, S., ... Vernier, J. P. (2014). Total volcanic stratospheric aerosol optical depths and implications for global climate change. *Geophysical Research Letters*, *41*, 7763–7769.

Robock, A. (2000). Volcanic eruptions and climate. *Reviews of Geophysics*, *38*, 191-220. doi: 10.1029/1998RG000054

Russell, P., Livingston, J., Pueschel, R., Bauman, J., Pollack, J., Brooks, S., ... Bergstrom, R. (1996). Global to microscale evolution of the Pinatubo volcanic aerosol derived from diverse measurements and analyses. *J. Geophys. Res. D.*, *101*(13), 18.

Schoeberl, M., Wang, Y., Ueyama, R., Taha, G., Jensen, E., & Yu, W. (2022). Analysis and Impact of the Hunga Tonga-Hunga Ha'apai Stratospheric Water Vapor Plume. *Geophysical Research Letters*, *49*(20), e2022GL100248.

Seinfeld, J., & Pandis, S. N. (2012). *Atmospheric chemistry and physics: from air pollution to climate change.* New Jersey, USA: John Wiley and Sons.

Sellitto, P., Podglajen, A., Belhadji, R., Boichu, M., Carboni, E., Cuesta, J., ... others (2022). The unexpected radiative impact of the Hunga Tonga eruption of 15th January 2022. *Communications Earth & Environment*, *3*(1), 1–10.

Sinyuk, A., Holben, B. N., Eck, T. F., Giles, D. M., Slutsker, I., Korkin, S., ... Lyapustin, A. (2020). The AERONET Version 3 aerosol retrieval algorithm, associated uncertainties and comparisons to Version 2. *Atmospheric Measurement Techniques Discussions*, *12*, 1–80.

Sioris, C., Boone, C., Bernath, P., Zou, J., McElroy, C., & McLinden, C. (2010). Atmospheric chemistry experiment (ace) observations of aerosol in the upper troposphere and lower stratosphere from the kasatochi volcanic eruption. *Journal of Geophysical Research: Atmospheres*, *115*(D2).

Solomon, S. (1999). Stratospheric ozone depletion: A review of concepts and history. *Reviews of Geophysics*, *37*(3), 275–316.

Stothers, R. B. (2001). A chronology of annual mean effective radii of stratospheric aerosols from volcanic eruptions during the twentieth century as derived from ground-based spectral extinction measurements. *Journal of Geophysical Research: Atmospheres*, *106*(D23), 32043–32049.

Taha, G., Loughman, R., Colarco, P., Zhu, T., Thomason, L., & Jaross, G. (2022). Tracking the 2022 Hunga Tonga-Hunga Ha'apai Aerosol Cloud in the Upper and Middle Stratosphere Using Space-Based Observations. *Geophysical Research Letters*, *49*(19), e2022GL100091.

Taha, G., Loughman, R., Zhu, T., Thomason, L., Kar, J., Rieger, L., & Bourassa, A. (2021). OMPS LP Version 2.0 multi-wavelength aerosol extinction coefficient retrieval algorithm. *Atmospheric Measurement Techniques*, *14*(2), 1015–1036.

Tanré, D., Kaufman, Y., Holben, B. e. a., Chatenet, B., Karnieli, A., Lavenu, F., ... Smirnov, A. (2001). Climatology of dust aerosol size distribution and optical properties derived from remotely sensed data in the solar spectrum. *Journal of Geophysical Research: Atmospheres*, *106*(D16), 18205–18217.

Textor, C., Graf, H. F., Herzog, M., Oberhuber, J. M., Rose, W. I., & Ernst, G. G. J. (2006). Volcanic particle aggregation in explosive eruption columns. Part II:

Numerical experiments. *Journal of Volcanology and Geothermal Research*, *150*, 378-394. doi: 10.1016/j.jvolgeores.2005.09.008

Theys, N., De Smedt, I., Yu, H., Danckaert, T., van Gent, J., Hörmann, C., ... others (2017). Sulfur dioxide retrievals from TROPOMI onboard Sentinel-5 Precursor: algorithm theoretical basis. *Atmospheric Measurement Techniques*, *10*(1), 119–153.

Theys, N., Hedelt, P., De Smedt, I., Lerot, C., Yu, H., Vlietinck, J., ... others (2019). Global monitoring of volcanic SO2 degassing with unprecedented resolution from TROPOMI onboard Sentinel-5 Precursor. *Scientific reports*, *9*(1), 1–10.

Thomason, L. W., Kovilakam, M., Schmidt, A., Von Savigny, C., Knepp, T., & Rieger, L. (2021). Evidence for the predictability of changes in the stratospheric aerosol size following volcanic eruptions of diverse magnitudes using space-based instruments. *Atmospheric Chemistry and Physics*, *21*(2), 1143–1158.

Tilmes, S., Müller, R., & Salawitch, R. (2008). The sensitivity of polar ozone depletion to proposed geoengineering schemes. *Science*, *320*(5880), 1201–1204.

Timmreck, C., Graf, H.-F., Lorenz, S. J., Niemeier, U., Zanchettin, D., Matei, D., ... Crowley, T. J. (2010). Aerosol size confines climate response to volcanic super-eruptions. *Geophysical Research Letters*, *37*(24).

Timmreck, C., Lorenz, S. J., Crowley, T. J., Kinne, S., Raddatz, T. J., Thomas, M. A., & Jungclaus, J. H. (2009). Limited temperature response to the very large AD 1258 volcanic eruption. *Geophysical Research Letters*, *36*(21).

Torres, B., Dubovik, O., Toledano, C., Berjón, A., Cachorro, V. E., Lapyonok, T., ... Goloub, P. (2014). Sensitivity of aerosol retrieval to geometrical configuration of ground-based sun/sky radiometer observations. *Atmospheric Chemistry and Physics*, *14*(2), 847–875.

Vernier, J.-P., Timmreck, C., & Kremser, S. (2022). *Atmospheric impacts of the 2022 Hunga Tonga-Honga Ha'apai (HT-HH) eruption* (Tech. Rep.). SPARC SSiRC community. Retrieved from `www.sparc-ssirc.org/downloads/VolRes_summary_of_the_Hunga-Vfinal.pdf`

Vömel, H., Evan, S., & Tully, M. (2022). Water vapor injection into the stratosphere by Hunga Tonga-Hunga Ha'apai. *Science*, *377*(6613), 1444–1447.

Wang, X., Randel, W., Zhu, Y., Tilmes, S., Starr, J., Yu, W., ... others (2022). Stratospheric climate anomalies and ozone loss caused by the Hunga Tonga volcanic eruption. *Authorea Preprints*. Retrieved from `https://www.authorea.com/doi/full/10.1002/essoar.10512922.1` doi: 10.1002/essoar.10512922.1

Winker, D. M., Vaughan, M. A., Omar, A., Hu, Y., Powell, K. A., Liu, Z., ... Young, S. A. (2009). Overview of the CALIPSO mission and CALIOP data processing algorithms. *Journal of Atmospheric and Oceanic Technology*, *26*(11), 2310–2323.

Wrana, F., Von Savigny, C., Zalach, J., & Thomason, L. W. (2021). Retrieval of stratospheric aerosol size distribution parameters using satellite solar occultation measurements at three wavelengths. *Atmospheric Measurement Techniques*, *14*(3), 2345–2357.

Zhu, Y., Bardeen, C. G., Tilmes, S., Mills, M. J., Wang, X., Harvey, V. L., ... others (2022). Perturbations in stratospheric aerosol evolution due to the water-rich plume of the 2022 Hunga-Tonga eruption. *Communications Earth & Environment*, *3*(1), 1–7.

Supporting Information for "Growth and global persistence of stratospheric sulfate aerosols from the 2022 Hunga Tonga-Hunga Haápai volcanic eruption"

Marie Boichu[1,2], Raphaël Grandin[3], Luc Blarel[1,2], Benjamin Torres[2], Yevgeny Derimian[1,2], Philippe Goloub[2], Colette Brogniez[2], Isabelle Chiapello[1,2], Oleg Dubovik[1,2], Théo Mathurin[4], Nicolas Pascal[1,4], Maximilien Patou[4], Jérôme Riedi[2,4]

[1]CNRS, UMR 8518, F-59000 Lille, France

[2]University of Lille, UMR 8518 - LOA - Laboratoire d'Optique Atmosphérique, F-59000 Lille, France

[3]Université Paris Cité, Institut de Physique du Globe de Paris, CNRS, 75005 Paris, France

[4]University of Lille, CNRS, CNES, UMS 2877 – ICARE Data and Services Center, F-59000 Lille, France

Contents of this file

1. Figures S1 to S12.
2. Movie S1.

Additional Supporting Information (Files uploaded separately)

Corresponding author: M. Boichu, CNRS/University of Lille, UMR 8518 - LOA - Laboratoire d'Optique Atmosphérique, F-59000 Lille, France. (marie.boichu@univ-lille.fr)

1. Caption for Movie S1: Animation of HIMAWARI-8/AHI SO_2 RGB composition from 15 January 00:00 to 17 January 2022 07:00 UTC that illustrates the transport and dispersion of the HT-HH plume from source to Australia. Animation made using the VOLCPLUME portal (Boichu & Mathurin, 2022).

Movie S1. Animation of HIMAWARI-8/AHI SO_2 RGB composition from 15 January 00:00 to 17 January 2022 07:00 UTC that illustrates the transport and dispersion of the HT-HH plume from source to Australia. Animation made using the VOLCPLUME portal (Boichu & Mathurin, 2022).

References

Boichu, M., & Mathurin, T. (2022). *VOLCPLUME, an interactive web portal for the multiscale analysis of volcanic plume physico-chemical properties* [Interactive Web-based Ressource]. Direct access: https://volcplume.aeris-data.fr. Retrieved August 2023, from `https://www.icare.univ-lille.fr/volcplume/` doi: 10.25326/362

Holben, B., Setzer, A., Eck, T., Pereira, A., & Slutsker, I. (1996). Effect of dry-season biomass burning on Amazon basin aerosol concentrations and optical properties, 1992–1994. *Journal of Geophysical Research: Atmospheres*, *101*(D14), 19465–19481.

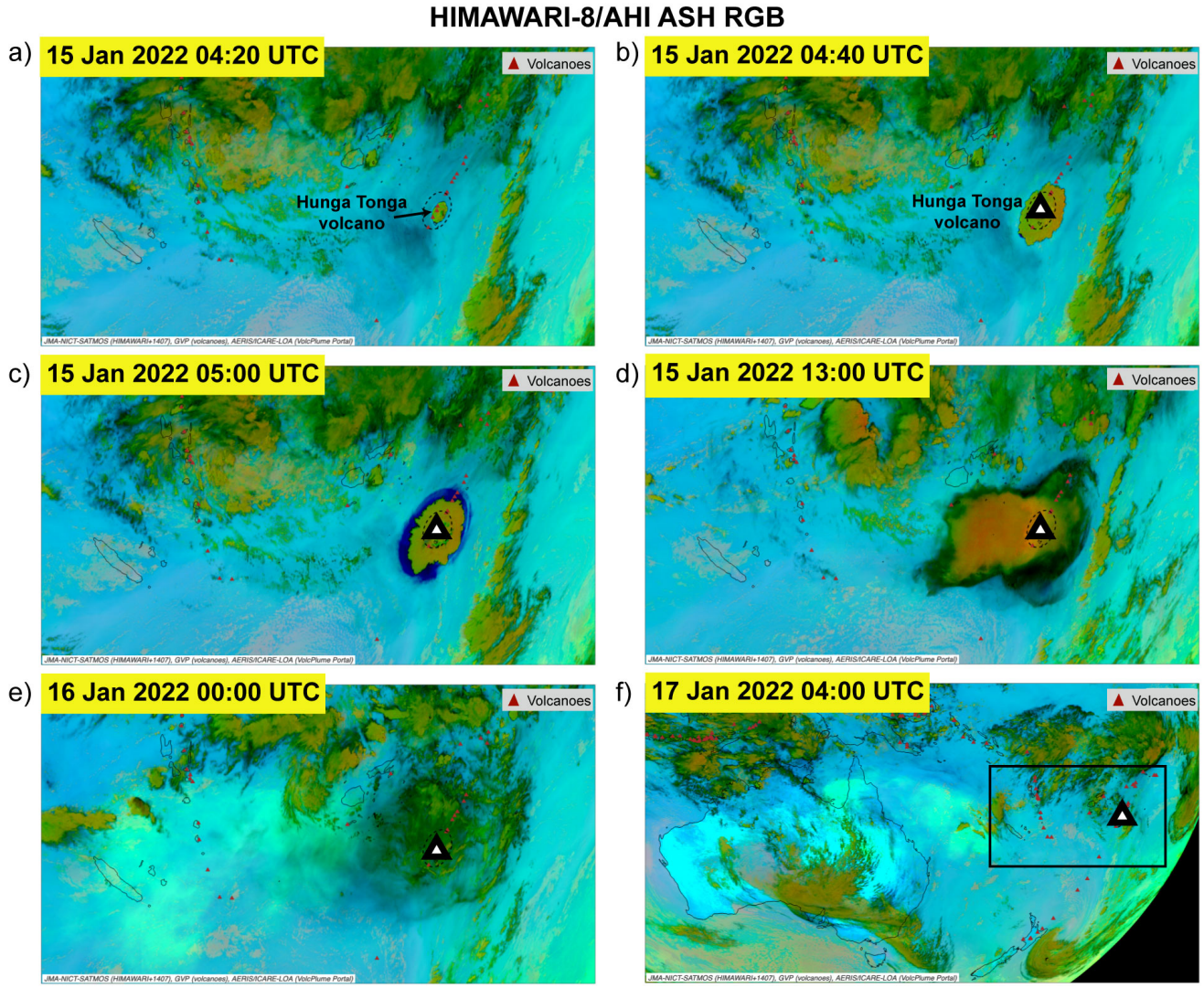

Figure S1: Ash RGB products from HIMAWARI-8/AHI satellite observations of the near-source plume from Hunga Tonga-Hunga Haápai volcano (triangle) from (a) 15 January 2022 04:20 UTC (first detection of HT-HH plume) to (f) 17 January 2022 04:00 UTC. Note the extended geographical area in (f) with a black rectangle that indicates the more restricted zone covered in subfigures a to e.

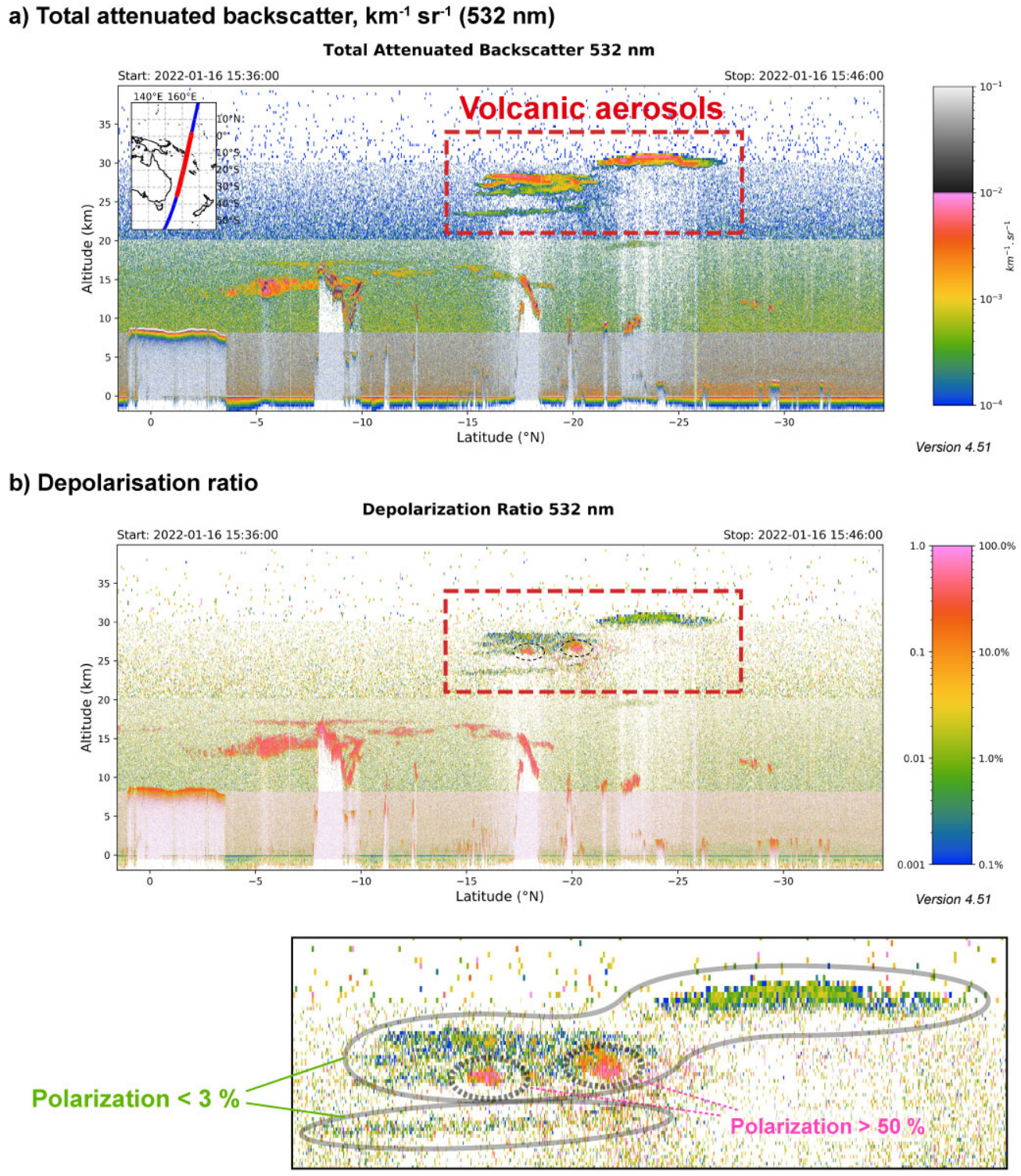

Figure S2: Detection of HT-HH aerosols (contoured in red) with CALIPSO/CALIOP Level 1 observations (Version 4.51) along the track passing near the eastern coast of Australia on 16 January 2022 from 15:36 to 15:46 UTC (red line in inset). (a) Total attenuated backscatter at 532 nm, (b) depolarisation ratio at 532 nm. The bottom panel shows a zoom on the volcanic plume, indicating the predominance of poorly-depolarizing aerosols (blue-green, area surrounded by solid line), and the presence of secondary, isolated parcels with depolarizing properties (pink, area surrounded by dashed line).

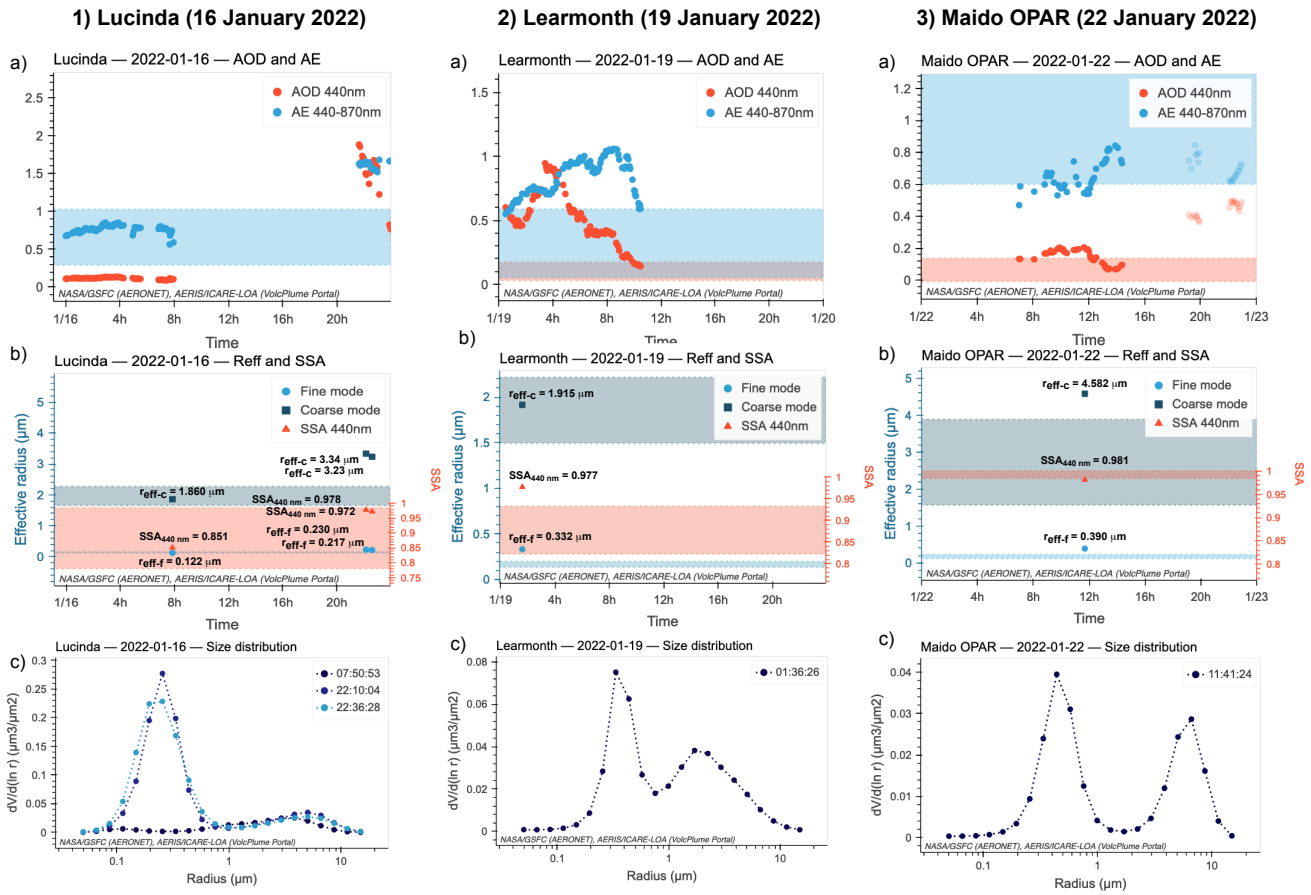

Figure S3: Detailed optical and absorption properties of particles derived from almucantar observations at the AERONET stations of (1) Lucinda (eastern Australia) on 16 January 2022, (2) Learmonth (western Australia) on 19 January 2022 and (3) Maido OPAR (La Réunion island) on 22 January 2022. Time series (in UT) of (a) AOD_{440nm} (red) and Angstrom exponent AE (440-870 nm, blue), (b) effective radius of fine (light blue circles) and coarse (dark blue squares) aerosols (left axis) as well as the single scattering albedo (SSA) at 440 nm (red triangles, right axis). The shaded areas indicate the range of historical monthly-mean values for each parameter (mean $\pm 1\sigma$) over the ± 15 days around the date of interest. (c) Aerosol volume size distribution.

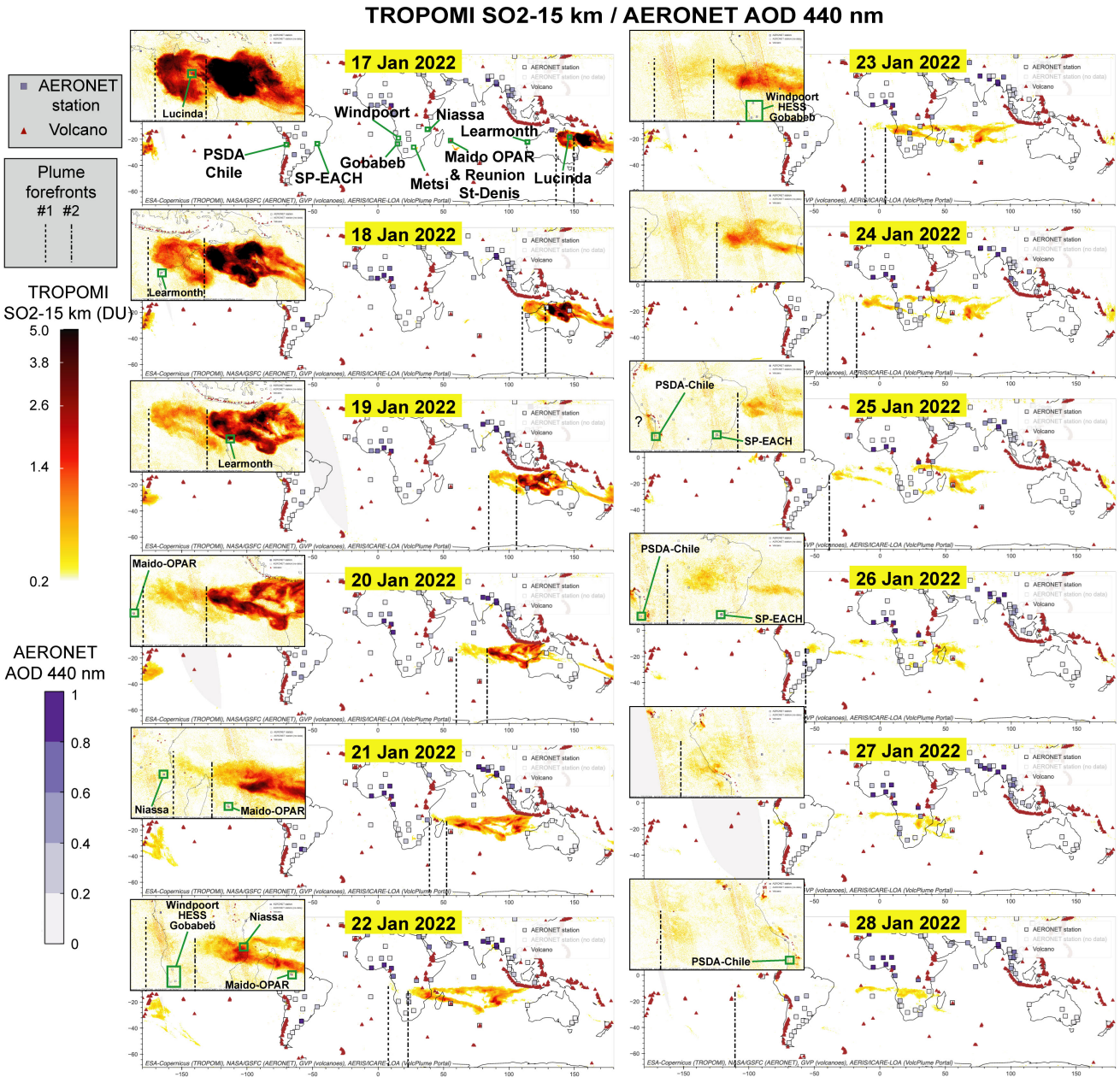

Figure S4: Dispersion of the HT-HH SO_2-rich plume (column amounts > 0.2 DU) from Australia toward South America in January 2022 from TROPOMI observations (15 km product). The location of AERONET stations is indicated by square symbols with blue color proportional to daily AOD_{440nm} values. Stations that are extensively explored for the growth of sulfate aerosols along plume transport during the first circumnavigation of the globe are contoured in green in the top panels. Dashed vertical lines indicate two forefronts of the SO_2 plume as long as they can be identified unambiguously, based on visual interpretation. Two different plume fronts are distinguished (dashed line: first plume front ; dash-dotted line: second plume front). Note that this tracking is not intended to be quantitative, but aims at illustrating qualitatively the advance of the two fronts of the plume, in order to facilitate the attribution of anomalies at ground stations to the HT-HH eruption. Insets show zooms to justify the tracking.

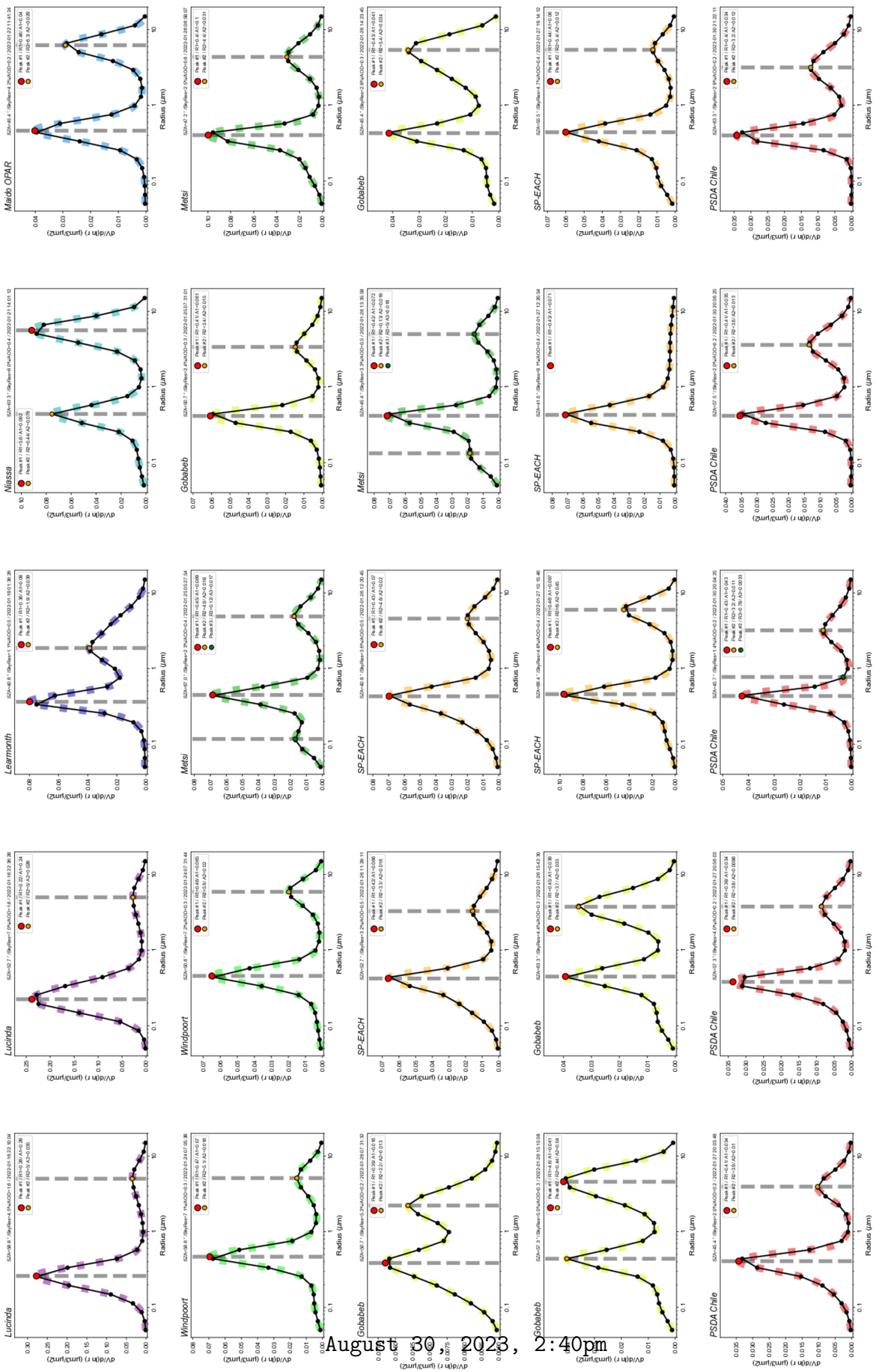

Figure S5: Aerosol volume size distributions of all measurements shown in Fig. 5 (main text).

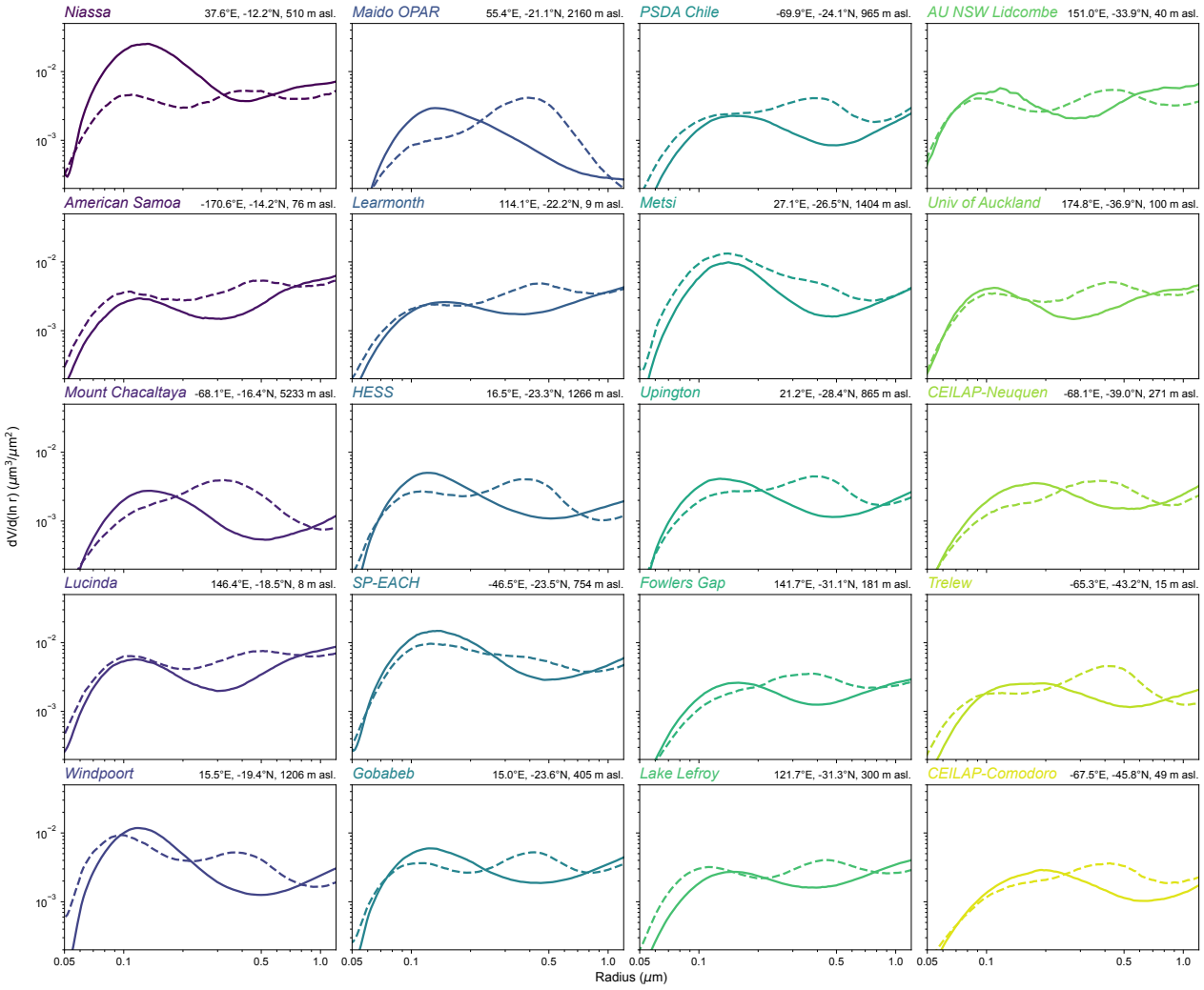

Figure S6: Median of the aerosol volume size distributions over 20 AERONET stations of the southern hemisphere before (eg. from January 2020 to January 2022, thick line) and after (eg. January 2022 to May 2023, dashed line) the HT-HH eruption, displayed in the fine mode range, for the subset of VSDs with $r_{peak,1}$<0.90 μm or $r_{peak,2}$<0.90 μm (ie. those including either their largest or second-largest peak in the fine mode range). The color of station symbol varies with latitude, as shown in the map of Fig. 7.

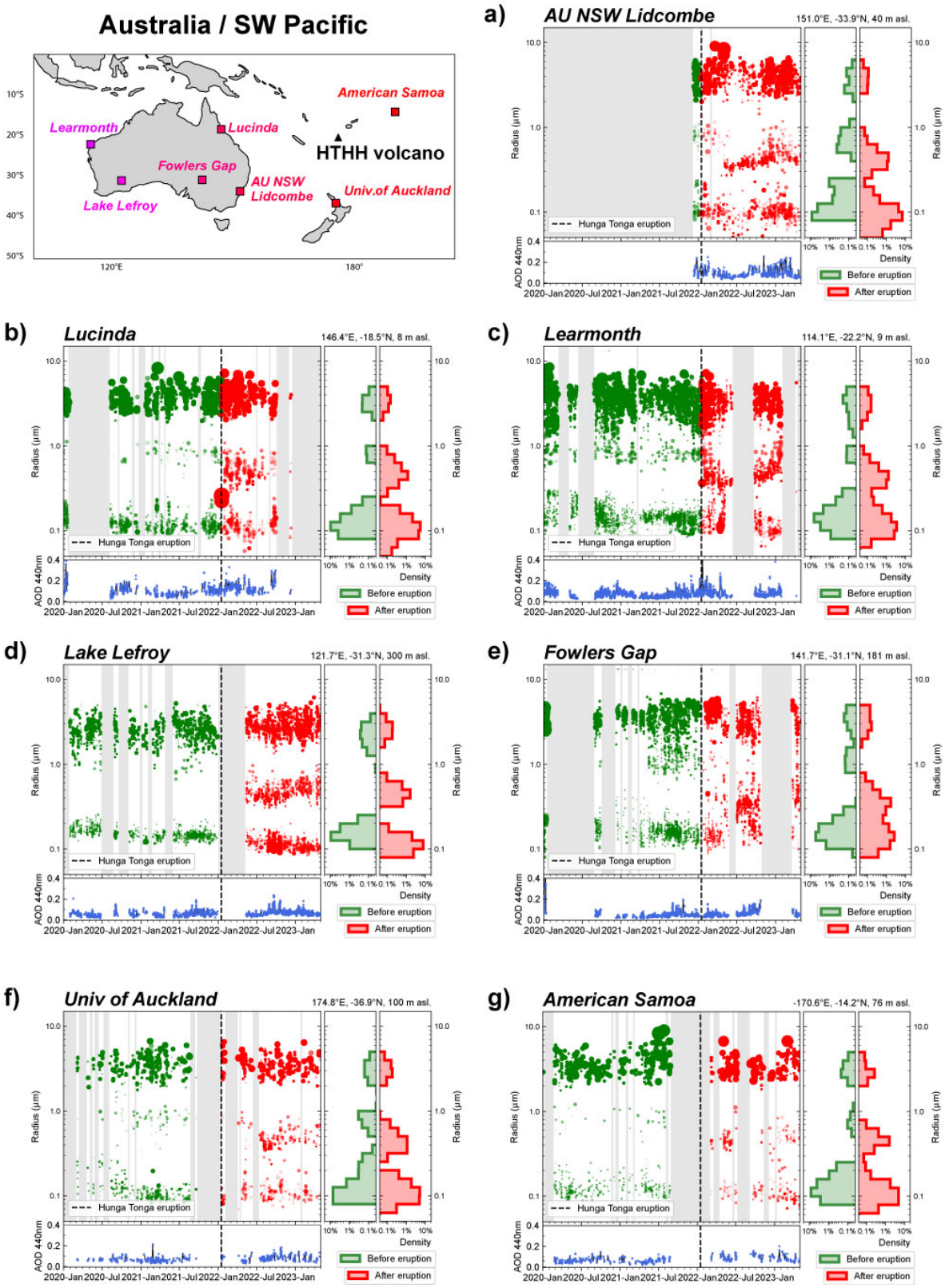

Figure S7: Time series from 1 January 2020 to 1 May 2023 at Australian and SW Pacific stations of (a) AU NSW Lidcombe, (b) Lucinda, (c) Learmonth, (d) Lake Lefroy and (e) Fowlers Gap, (f) New Zealand/Univ. of Auckland, (g) American Samoa, of (top left) both fine/coarse aerosol r_{peak} values with (top right) associated histograms (red/green symbols are respectively associated to data before/after the HT-HH eruption indicated by a vertical dashed line) and (bottom) AOD_{440nm} (data in blue, black line for 3 day-running average with no gap filling). r_{peak} correspond to local maxima of the spline interpolation of the column-integrated volume size distribution. Symbol size is proportional to the aerosol volume concentration and symbol opacity is divided in three classes (1^{st} highest peak in spline interpolation of VSD, corresponding to the size of aerosols contributing the most to the volume concentration, is associated to an opacity of 100%, 2^{nd} peak: 60% opacity, 3^{rd} peak: 20% opacity). Histograms represent the frequency density of r_{peak} in each VSD.

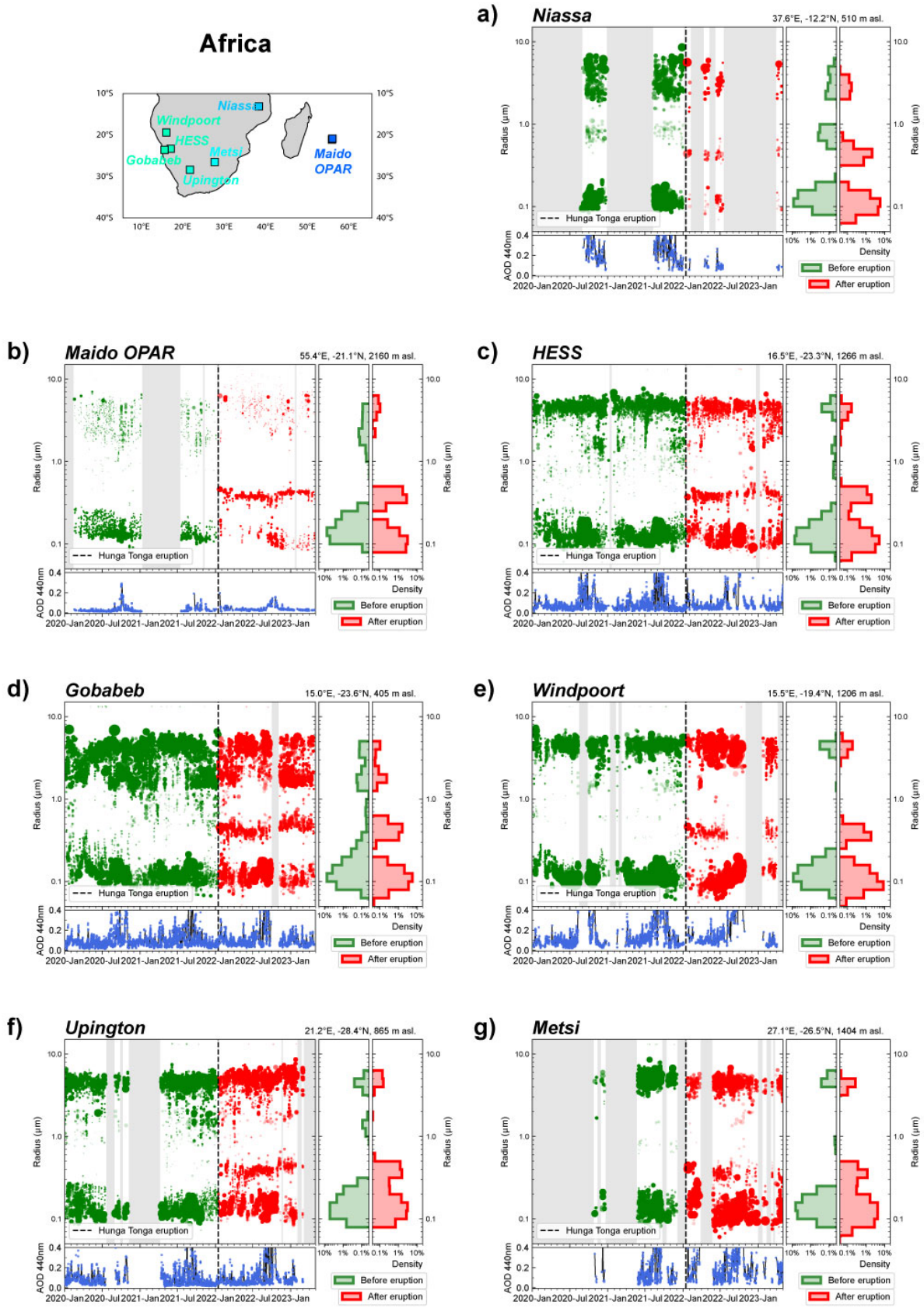

Figure S8: Same as Fig. S7 for AERONET stations in southern Africa: (a) Mozambique/Niassa, (b) western Indian Ocean/La Réunion/Maido OPAR and (c) Namibia/HESS, (d) Namibia/Gobabeb, (e) Namibia/Windpoort, (f) South Africa/Upington, (g) South Africa/Metsi.

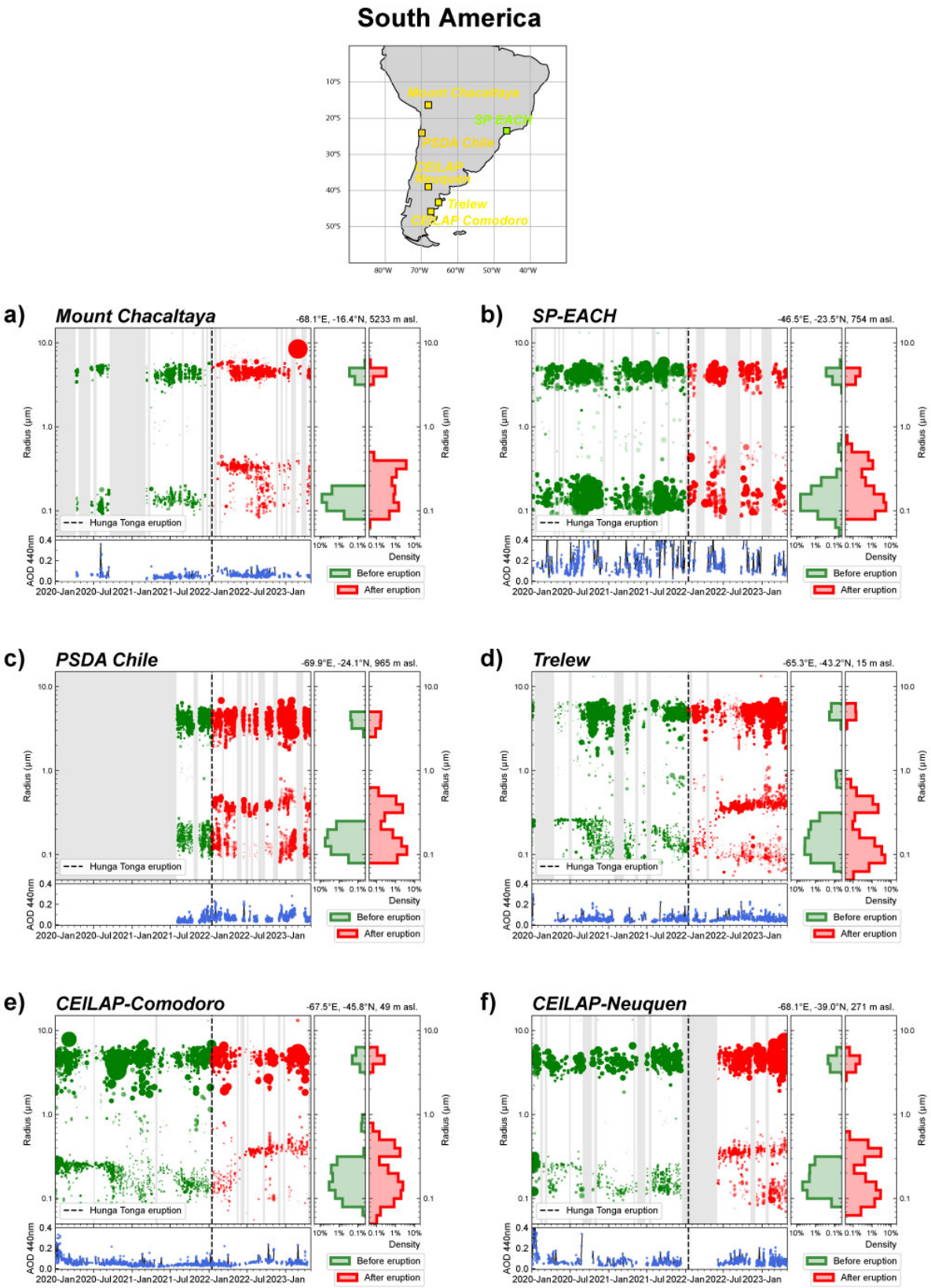

Figure S9: Same as Fig. S7 for AERONET stations in South America: (a) Bolivia/Mount Chacaltaya, (b) Brazil/SP-EACH, (c) Chile/PSDA Chile, (d) Argentina/Trelew, (e) Argentina/CEILAP-Comodoro, (f) Argentina/CEILAP-Neuquen.

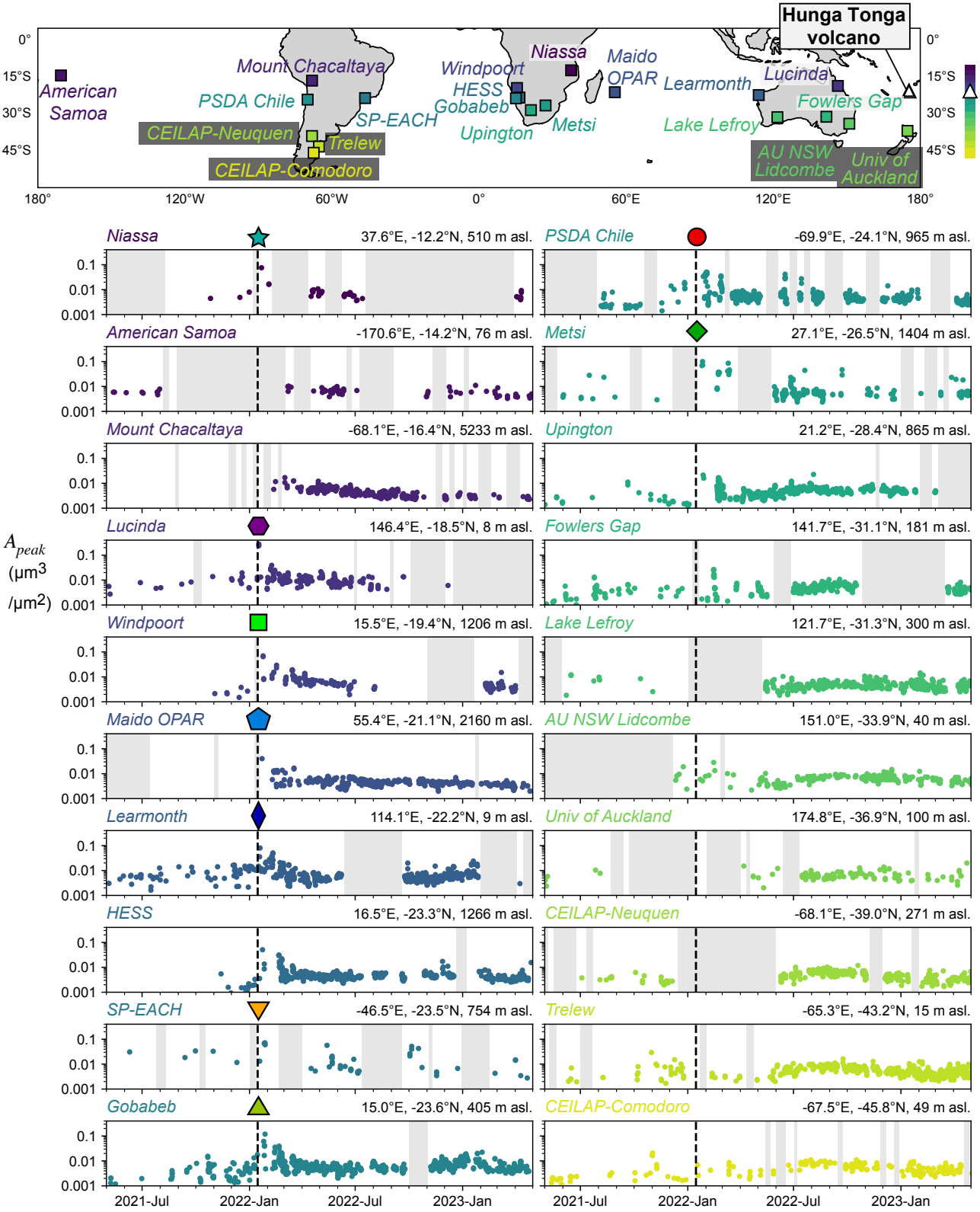

Figure S10: Amplitude of aerosol volume size distribution at the r_{peak} radius value associated with the HT-HH volcanic fine mode (illustrated in Fig. 7 of the main text), from May 2021 to May 2023, at 20 AERONET stations of the southern hemisphere. The color of station symbol varies with latitude. Grey areas indicate data gaps longer than 15 days. HT-HH eruption is indicated by dashed vertical line. August 30, 2023, 2:40pm

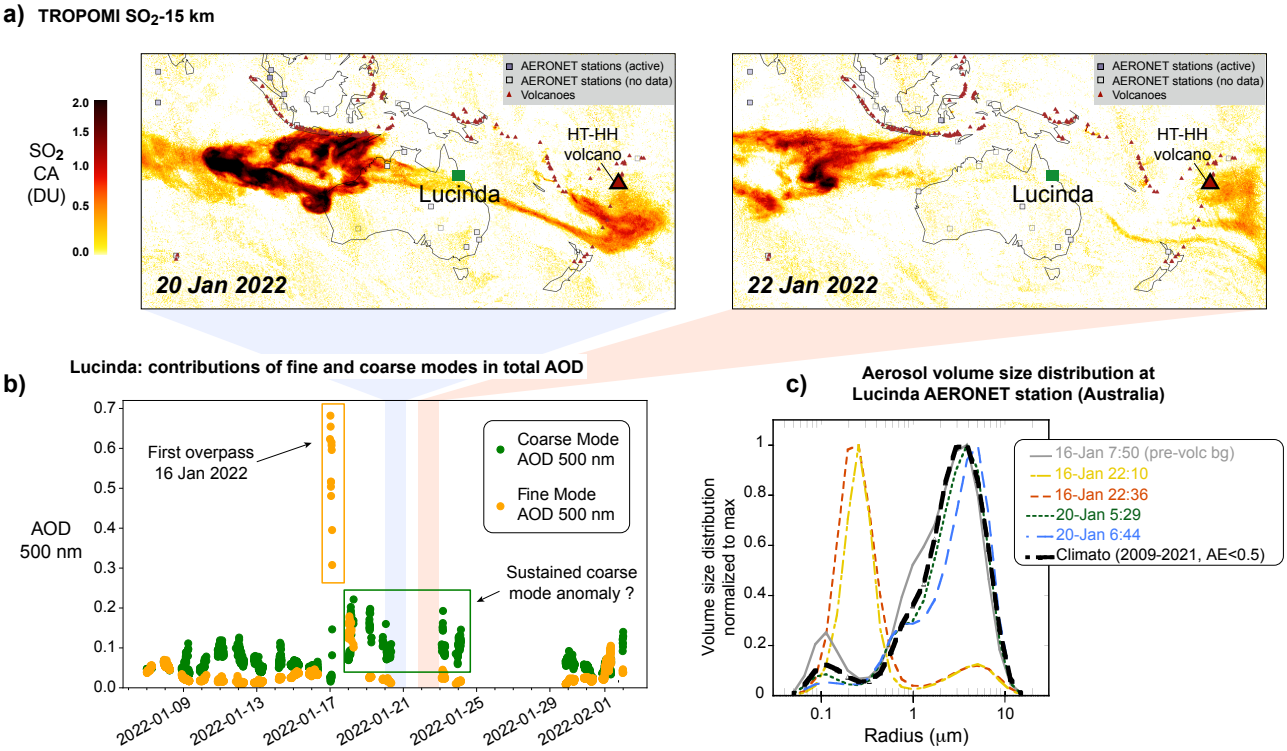

Figure S11: (a) Dispersion of the HT-HH SO_2 plume with TROPOMI observations (15 km product) from 20 to 22 January 2022, with indication of the location of the AERONET photometric station of Lucinda in Eastern Australia (green square). (b) Time series of fine (yellow) and coarse (green) mode contribution to AOD_{500nm} (SDA algorithm) in January 2022. (c) Comparison of the volume size distribution (VSD) of aerosols derived from almucantar observations of the atmospheric column over Lucinda: before the arrival of the HT-HH plume on 16 January 07:50 UTC (grey), during the passing of the forefront of the plume on 16 Jan at 22:10 (yellow) and 22:36 UTC (orange) and during the overpass by the tail of the plume on 20 Jan at 05:29 (green) and 06:44 UTC (blue). Mean VSD from a climatological analysis over 13 years (from 2009 to 2021, Angström exponent < 0.5 to select data with abundant coarse particles) in black dashed line.

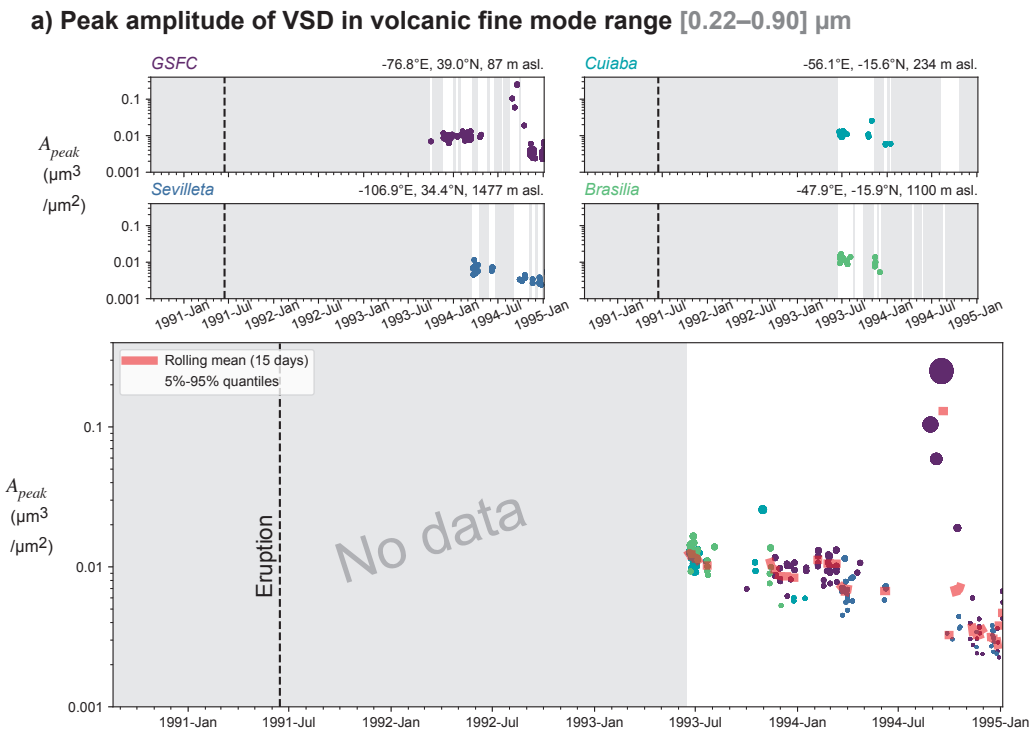

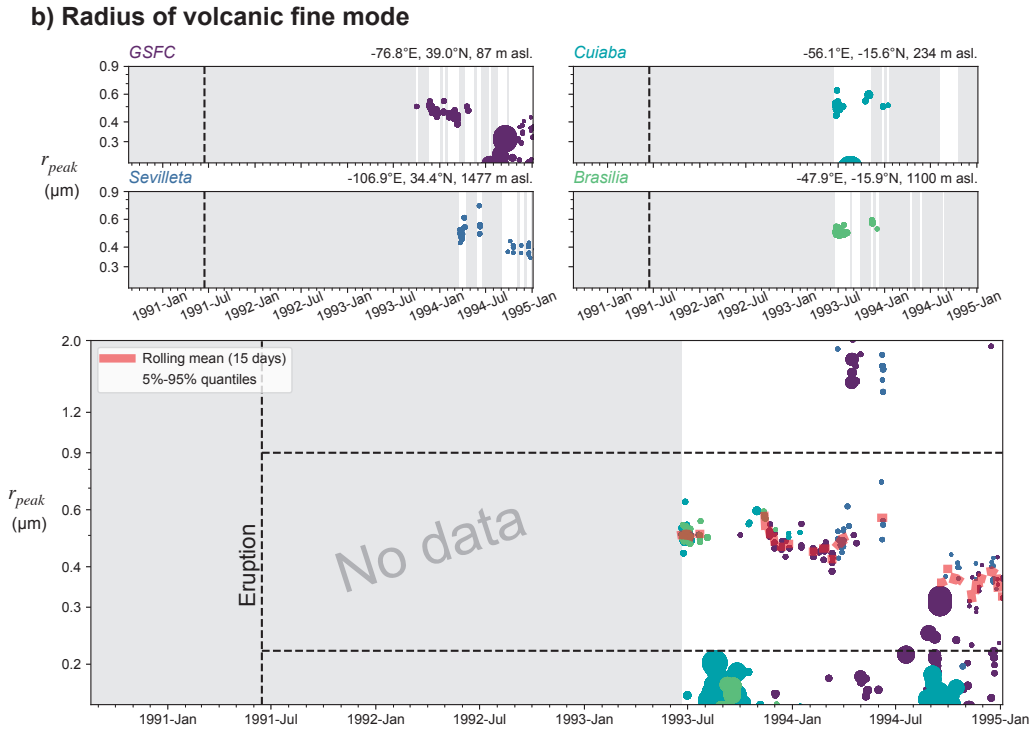

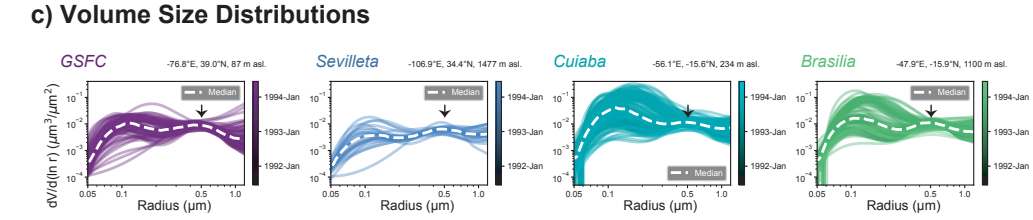

August 30, 2023, 2:40pm

Figure S12: AERONET analysis of aerosol size following the 15 June 1991 Pinatubo eruption for 4 selected stations: GSFC (USA), Sevilleta (USA), Cuiaba (Brazil) and Brasilia (Brazil). Note that stations GSFC and Cuiaba correspond to the dataset used by Holben et al. (1996). (a) Time-series of aerosol peak amplitudes A_{peak} for individual stations (top) and stacked (bottom). Red line is the 15-days rolling mean (same representation and criteria as in Fig. 8a). Vertical dashed line marks the time of the eruption. (b) Time-series of aerosol peak radius $r_{peak,i}$ (with i=1,2) for individual stations (top) and stacked (bottom). Red line is the 15-days rolling mean represented in Fig. 8c and 8d (same representation and criteria as in Fig 8b). (c) Post-eruption aerosol volume size distributions for individual stations (same representation and criteria as in Fig 6a). Black arrows mark the location of the peak of the "volcanic middle mode".